

1 The Response of the Northwest Atlantic Ocean to Climate Change

2
3 Michael A. Alexander¹, Sang-ik Shin^{1,2}, James D. Scott^{1,2}, Enrique Curchitser³, Charles Stock⁴

4
5 1 - NOAA/Earth System Research Laboratory, Boulder, Colorado

6 2 - Cooperative Institute for Research in Environmental Sciences, University of Colorado
7 Boulder, Boulder, Colorado

8 3 - Department of Environmental Sciences, Rutgers, The State University of New Jersey, New
9 Brunswick, New Jersey

10 4 - NOAA/Geophysical Fluid Dynamics Laboratory, Princeton, New Jersey

11
12
13
14 Manuscript submitted to the Journal of Climate, February 2019

15 Revised June 2019, 2nd Revision August 2019

16
17
18
19 Corresponding Authors Address:
20 Michael Alexander
21 NOAA, Earth System Research Laboratory
22 R/PSD1
23 325 Broadway
24 Boulder, CO 80305-3328
25 Michael.Alexander@noaa.gov

26
27
28
29
30
31
32
33
34
35
36
37
38
39
40
41
42
43
44
45

Abstract

ROMS, a high-resolution regional ocean model, was used to study how climate change may affect the northwest Atlantic Ocean. A control (CTRL) simulation was conducted for the recent past (1976-2005), and simulations with additional forcing at the surface and lateral boundaries, obtained from three different global climate models (GCMs) using the RCP8.5 scenario, were conducted to represent the future (2070-2099). The climate change response was obtained from the difference between the CTRL and each of the three future simulations.

All three ROMS simulations indicated large increases in sea surface temperatures (SSTs) over most of the domain except off the eastern US seaboard due to weakening of the Gulf Stream. There are also substantial inter-model differences in the response, including a southward shift of the Gulf Stream in one simulation and a slight northward shift in the other two, with corresponding changes in eddy activity. The depth of maximum warming varied among the three simulations, resulting in differences in the bottom temperature response in coastal regions, including the Gulf of Maine and the west Florida Shelf. The surface salinity decreased (increased) in the northern (southern) part of the domain in all three experiments, but in one, the freshening extended much further south in ROMS than in the GCM that provided the large-scale forcing, associated with changes in the well resolved coastal currents. Thus, while high resolution allows for a better representation of currents and bathymetry, the response to climate change can vary considerably depending on the large-scale forcing.

46 **1. Introduction**

47 The increase in greenhouse gasses over the past century has contributed to the warming of
48 most of the world's oceans, including highly productive coastal regions responsible for the
49 vast majority of global fish catch (e.g. Pauly and Zeller 2016). For example, Belkin (2009)
50 found that 61 of the 63 large marine ecosystems (LMEs) that are mainly located in coastal
51 regions exhibited warming from 1982–2006, while Lima and Wetthey (2012) found that ~3/4
52 of coastal areas experienced an increase in SST, with an overall rate of $0.25^{\circ}\text{C dec}^{-1}$, from 1982
53 to 2010. While broad warming due to accumulating greenhouse gasses is likely to continue,
54 these trends may be significantly exacerbated (or ameliorated) by regional processes such as
55 the retreat of sea ice, changes in finer-scale features, such as fronts and eddies, and the effects
56 of small-scale coastal/bathymetric features on the response to climate change. Given that
57 complex ocean current systems and highly productive marine ecosystems are often located
58 near land, where climate change induced warming is expected to be more intense, greenhouse
59 gas induced changes may have an especially pronounced effects in coastal areas. This could
60 well be the case for the US east coast and Gulf of Mexico, given the proximity of the Labrador
61 Current, Gulf Stream, and Loop current, and complex bathymetric features such as the
62 Laurentian Channel, Gulf of Maine, Georges Bank and west Florida Shelf (Fig. 1). Climate
63 change will not only influence SST but also temperature, salinity and currents throughout the
64 water column, which can subsequently impact marine ecosystems. Thus, models and datasets
65 with high spatial resolution may be necessary to fully diagnose and simulate the effects of
66 climate change in the northwest Atlantic and Gulf of Mexico.

67 Consistent with the potential for regional dynamics to shape large-scale warming patterns,
68 observational analyses indicate a range in SST trends along the east coast of North America.

69 Belkin (2009) found moderate to strong warming for the Scotian Shelf, moderate warming in
70 the Gulf of Mexico and modest warming on the NE and SE US shelf between 1982 and 2006,
71 although the warming was quite strong for the NE US over the longer period of 1957-2006.
72 Analyses of observations directly adjacent to the coast suggest weak cooling in the southeast
73 and somewhat stronger warming for the northeast US coast (Shearman and Lentz 2010, Lima
74 and Wethey 2012), where Gulf of Maine SST increased by more than 2°C between 2004 and
75 2013, nearly the largest increase over the global ocean during that period (Pershing et al. 2015).

76 Large changes are also projected for the North Atlantic Ocean in the future. Alexander et
77 al. (2018) found that SSTs increase by approximately 0.3°-0.4° C dec⁻¹ over the period 1976-
78 2099 for LMEs along the US east coast with even stronger warming of 0.5°C dec⁻¹ on the
79 Scotian Shelf based on simulations using the Representative Concentration Pathway 8.5
80 (RCP8.5) scenario from phase 5 of the Coupled Models Intercomparison Project (CMIP5)
81 archive. The very strong warming over the high latitude continents and the Arctic Ocean, i.e.
82 polar amplification, and the reduction in sea ice, likely contributes to changes over the Atlantic
83 through both the atmosphere and the ocean (e.g. Pedersen et al. 2016, Chen et al. 2014,
84 Coumou et al. 2018, Sun et al. 2018). In general, the models indicate that ocean warming is
85 greatest near the surface, which enhances the static stability, as does the surface freshening of
86 the Atlantic north of ~45°N (Capotondi et al. 2012). The enhanced stratification, particularly
87 at high latitude regions in the North Atlantic, reduces convection and slows the Atlantic
88 meridional overturning circulation (AMOC, e.g. Cheng et al. 2013; Collins et al. 2013). In
89 turn, changes in AMOC influence temperature and salinity (Drijfhout et al. 2012). In the
90 CMIP5 models, a decrease in AMOC is associated with cooling south of Greenland (“warming
91 hole”), warming southeast of Nova Scotia, decreased salinity in the subpolar gyre, and

92 increased salinity in the subtropical gyre, especially near the southeast US coast (Cheng et al.
93 2013). Changes in AMOC have the potential to alter basin-wide circulation patterns that impact
94 the physical/biological ocean response off the east coast of North America.

95 The resolution of the GCMs used in CMIP5 is relatively coarse, with an ocean resolution
96 on the order of 100 km, which does not resolve fine-scale topographic features and may not
97 adequately represent aspects of the ocean dynamics. For example, these models do not resolve
98 ocean eddies and simulate the separation of the Gulf Stream from the coast north of its observed
99 location at Cape Hatteras (e.g. Bryan et al. 2007), which can influence the response to
100 increasing greenhouse gases (Winton et al. 2014). Saba et al. (2016) investigated the response
101 of GCMs developed at the NOAA Geophysical Fluid Dynamics Laboratory (GFDL) with
102 varying atmosphere and ocean resolutions to a doubling of CO₂ (after an increase of 1% per
103 year). They found that the response to climate change varied with resolution, especially along
104 the northeast US coast, where the increase in temperature was much stronger in the simulation
105 with the finest resolution: 50 km in the atmosphere and 10 km in the ocean. At this resolution,
106 the SST warming off portions of the east coast exceeded 5°C, ~2.5 times greater than the
107 increase in the global mean and double that of the coarse resolution GCM. The warming was
108 especially strong in the Gulf of Maine, where very warm water from the Atlantic entered the
109 Gulf at depth through the northeast channel, which was only resolved in the highest resolution
110 simulation. The surface salinity increased along the most of the US east coast shelf, with strong
111 increases in bottom salinity along the North and South Carolina coast, and into the Gulf of
112 Maine and Scotian shelf via deep channels. Saba et al. (2016) attributed these changes in
113 temperature and salinity to a decrease in AMOC and a northward shift of the Gulf Stream.

114 While the projected changes in the Atlantic temperature, salinity and currents are generally
115 consistent with those observed to date (e.g. Boyer et al. 2005, Wu et al. 2012, Knutson et al.
116 2013, Ceaser et al. 2018), both the observed and simulated changes could reflect decadal
117 climate variability. In addition, there are large differences between models in their
118 representation of AMOC, other atmospheric and ocean processes, and their response to climate
119 change (e.g. Gregory et al. 2005, Danabasoglu 2008, Cheng et al. 2013, Karspeck et al. 2017),
120 and even small differences in the basin-scale response to climate change could result in large
121 differences in coastal regions. Thus, while the high-resolution GCM study of Saba et al. (2016)
122 is very informative, it is based on a highly idealized CO₂ scenario and represents just one
123 potential future for the North Atlantic Ocean. Since high-resolution global models are very
124 computationally intensive, an alternative approach is to dynamically downscale the large-scale
125 changes obtained from the GCM simulations using regional ocean models forced by GCM
126 output along their open ocean lateral boundaries and at the surface. Usually the GCM forcing
127 is bias corrected, removing the mean difference between the model and observations in the
128 historical period. Dynamically downscaled climate change simulations have been conducted
129 for several regions including the California Current System (Auad et al., 2006, Xiu et al. 2018),
130 the Bering Sea (Hermann et al. 2016), western North Pacific (Liu et al. 2016), Australian
131 boundary currents (Sun 2012) and the Caribbean/Gulf of Mexico (Liu et al. 2012, van
132 Hooidek et al. 2015; Liu et al. 2015). The regional model studies of the Gulf of Mexico
133 indicate weakening of the Loop Current and associated warm transient eddies, which reduces
134 the amount of anthropogenic warming especially in spring, while surface heating leads to
135 intense warming on the northeastern shelf in summer (Liu et al. 2015). The experiments
136 conducted by Liu et al. (2012, 2015), however, used a multi-GCM mean to drive a regional

137 ocean model, and thus retained only the linear component of the climate change forcing and
138 were not able to assess the range of the response.

139 Shin and Alexander (2019) examined the climate change response of a regional ocean
140 model in the northwest Atlantic including the Gulf of Mexico and off the US east coast. That
141 simulation was driven by output from the GFDL ESM2M model, a GCM in the CMIP5
142 archive, and indicated enhanced warming near the coast, including warming at depth in the
143 Gulf of Maine. Here we force the same regional model using fields from three different GCMs,
144 enabling us to generate a range of responses and test their robustness. We also examine a wide
145 range of variables including SST, bottom temperature, surface and bottom salinity, static
146 stability, currents and eddies, over much of the northwest Atlantic, from the western Caribbean
147 Sea to the Gulf of Saint Lawrence. We present the results for December-January-February
148 (DJF) and June-July-August (JJA), since the energetics of the Gulf Stream is seasonally
149 dependent (Kang et al. 2016) and the response to climate change can differ between winter and
150 summer (e.g. Alexander et al. 2018). The model and experiment design are described in section
151 2, the findings from the regional model are presented in section 3 and the results are
152 summarized and discussed in section 4.

153

154 **2. Models and Methods**

155 *a. Regional Ocean Model*

156 We used the Regional Ocean Modeling System (ROMS, Shchepetkin and McWilliams
157 2003, 2005) to investigate the effects of climate change on the northwest Atlantic. ROMS is a
158 terrain-following primitive equation model with a free surface using incompressible and
159 hydrostatic approximations. The version used here, configured by Kang and Curchitser (2013),

160 has a horizontal grid spacing of 7 km and 40 vertical sigma levels with higher resolution near
161 the surface. The domain extends along the east coast of North America from approximately
162 10°N to 52°N, covering the western Caribbean, Gulf of Mexico, and the western North Atlantic
163 from Florida to Newfoundland and includes the Loop Current, Florida Current, Gulf Stream
164 and the southern portion of the Labrador current (Fig. 1).

165 The initial and oceanic boundary forcing for the control (**CTRL**) ROMS simulation is
166 based on 5-day averages from the Simple Ocean Data Assimilation (SODA v2.1.6, archived
167 fields are on a 0.5° lat.-lon. grid with 40 vertical levels; Carton and Giese 2008), 6-hourly
168 surface forcing from the Co-ordinated Ocean–Ice Reference Experiments (CORE v2; ~1.9° lat.
169 -lon. resolution, Large and Yeager 2009) and daily fresh water flux from rivers from the
170 continental discharge data base (Dai et al. 2009). The initial conditions and forcing are bi-
171 linearly interpolated to the ROMS horizontal grid and linearly interpolated with depth (within
172 the Pyroms package), with radiational conditions for flow out of the domain and nudging of
173 temperature, salinity and in-flowing currents as a function of depth at the boundary. The CTRL
174 simulation is performed using the observed forcing over a 48-year period: 1958-2005. This
175 ROMS configuration well simulates the mean path of the Gulf Stream and the associated
176 distribution of eddy kinetic energy (Kang and Curchitser 2013, 2015), the circulation in the
177 Gulf of Maine (Shin and Alexander 2019), and temperatures on the continental shelf in the
178 mid-Atlantic Bight (Chen et al. 2018).

179

180 *b. Climate change simulations – “Delta Method”*

181 The large-scale climate change forcing is implemented using the “delta method”, where
182 the difference between *mean* conditions from a future and a recent period are added to

183 observations that vary with time during the recent period. Since the recent periods mean
184 climate and high-frequency variability is retained from observations, this method removes the
185 mean bias and retains realistic unforced climate variability over a range of time scales.
186 However, since the imposed climate change signal at the boundaries is still at a coarse
187 resolution, it does not allow for a change in variability in the future, and it assumes that the
188 mean climate state and the projected change are not highly correlated, i.e. the bias is not
189 strongly dependent on the mean climate state (e.g., Hare et al. 2012). Here, the delta (Δ) values
190 were obtained by subtracting the mean values during 1976-2005 from those in 2070-2099,
191 where the future period is simulated based on RCP8.5, representing the “business-as-usual”
192 scenario assuming little to no stabilization of greenhouse gas emissions by 2100. Since a key
193 aspect of this study is to perform a comprehensive analysis of multiple models, which is
194 computationally intensive, we chose to use the RCP8.5 scenario as it has the greatest increase
195 in greenhouse gases in IPCC AR5, and thus should have the largest signal-to-noise ratio.

196 The Δ s were computed for each calendar month and then interpolated to daily values,
197 which were then added to the CTRL initial ocean conditions and to the observed forcing during
198 each year of the CTRL simulation. Like the CTRL, the **RCP8.5** (CTRL + Δ forcing) ROMS
199 simulations are 48 years long. The ROMS response to the inclusion of GCM forcing is obtained
200 from the average of the RCP8.5 - CTRL values over the last 30 years of the simulation (1976-
201 2005 in the CTRL), allowing the model time (18 years) to spin-up to the additional forcing.

202 An additional benefit of the delta method is that since both the CTRL and the three
203 experiments use the same present day forcing, they include the same linear portion of any
204 model drift (although changes over time in the CTRL are expected due to observed changes in
205 the forcing). Indeed, local SST trends in the three experiments is substantially reduced after

206 subtracting out the CTRL trend. Trends are of both signs over the domain that nearly
207 compensate each other, indicating near-equilibrium conditions in a basin-wide sense (not
208 shown). However, even after subtracting out the trend values from the CTRL, local SST trends
209 still remain in the three experiments, especially in the HadGEM-ROMS simulation, where a
210 strong warming trend occurs off the mid-Atlantic coast (not shown). Thus, the model is still
211 adjusting and/or nonlinear process are creating local changes with time in response to the
212 repeat seasonal cycle forcing.

213 The surface fields from the GCMs needed to drive ROMS include near surface air
214 temperature and humidity, evaporation – precipitation (E-P), sea level pressure (SLP), zonal
215 and meridional winds, and the downwelling radiation at the surface. The necessary ocean fields
216 include sea surface height and temperature, salinity, zonal (u) and meridional (v) currents as a
217 function of depth. Freshwater flux Δs into the ocean from major rivers are applied at the
218 locations identified in the Dai et al. 2009 data base.

219 Choosing climate models to drive regional models is complicated by many factors (e.g.,
220 Knutti et al. 2019) including; *i*) natural variability, which can cause models and observations
221 to differ (e.g. Deser et al. 2014), especially in the Atlantic which exhibits strong inter-decadal
222 variability; *ii*) “the best” models can differ by which metrics are chosen (e.g. Gleckler et al.
223 2008; Overland et al. 2011); *iii*) models that most closely match observations in the present
224 climate may not be the best at simulating long-term trends and thus the response to climate
225 change (Jun et al. 2008) and *iv*), many models had similar origins and thus are not truly
226 independent (Sanderson et al. 2015). Thus, we do not attempt to use a multi-model mean or
227 to define the best models, rather we use three different model simulations under the RCP8.5
228 climate scenario to investigate the *sensitivity* of their response to strong forcing.

229 The Δ values used to initialize and drive ROMS were obtained from GCMs used in the
230 fifth IPCC assessment: the GFDL ESM2M, Institute Pierre Simon Laplace (IPSL) CM5A-MR,
231 and the Hadley Center HadGEM2-CC (HadGEM). These models were chosen in part due to
232 their differences in AMOC in both their climatology and response to anthropogenic forcing
233 and the magnitude of their transient climate response in global surface temperature (Table 1).
234 For example, the transient climate response is weak, moderate and strong, in the GFDL, IPSL
235 and HadGEM models, respectively. In addition, all three are earth system models and thus
236 could provide the necessary forcing fields in future downscaling experiments that include
237 ocean biogeochemistry.

238

239 **3. Results**

240 *a Temperature*

241 The SST response to projected climate change (RCP8.5 – CTRL, shading in Fig. 2)
242 includes warming over nearly the entire domain in both winter (DJF) and summer (JJA) for
243 the three GCM-driven ROMS simulations that are subsequently referred to as GFDL-ROMS,
244 IPSL-ROMS and HadGEM-ROMS. The warming is lessened in and to the south of the Gulf
245 Stream front, as indicated by the region of strong temperature gradients (contours from the
246 CTRL in Fig. 2), during DJF in all three ROMS simulations. This reduced warming is primarily
247 due to changes in the meridional ocean heat transport. As the Gulf Stream slows in the future
248 (see section 3e), i.e. the response opposes the mean current, it transports less heat northward
249 off the southeast US coast (Fig. 1 in the Supplementary Material, Fig. SM1). From a heat
250 budget perspective, the change in the surface currents times the mean SST gradient is negative,
251 which acts to cool the SSTs (Fig. SM1). While this process occurs in all three simulations, it

252 is especially strong in the GFDL-ROMS experiment. Cooling due to the change in heat
253 transport is weaker in summer than in winter in all three ROMS simulations, mainly due to a
254 relaxing of the meridional SST gradient. Also during summer, a strong shallow mixed layer
255 forms and the surface layer is decoupled from the deeper ocean and resulting in stronger
256 thermodynamic air-sea coupling, reducing the effects of the change in heat transport on SST.

257 There are other notable differences among the three simulations. The IPSL-ROMS and
258 HadGEM-ROMS simulations exhibit very strong warming ($> 4^{\circ}\text{C}$) in the northwest part of the
259 domain, while the warming in GFDL-ROMS is on the order of 2°C . Enhanced coastal warming
260 relative to adjacent ocean waters is far more extensive in the HadGEM-ROMS simulation than
261 in the other models during winter, when it extends along the nearly the entire US coast and
262 into Canadian waters. The simulations, especially GFDL-ROMS and HadGEM-ROMS,
263 indicate very strong warming on the outer west Florida shelf during winter; while Liu et al.
264 (2015) also found enhanced warming in this region, it occurred on the inner shelf in summer.

265 The broad structure of the three SST responses in ROMS are driven by the basin-scale
266 changes as can be seen by relating the ROMS response to the changes in the corresponding
267 GCM. For example, like the ROMS simulations, the global models indicate reduced warming
268 in the Gulf Stream region and its extension into the North Atlantic (with a corresponding
269 decrease in the currents, section 3.e), especially in the GFDL GCM during winter (Fig. SM2).
270 The three GCMS also indicate intense warming of the surface air temperature over eastern
271 Canada especially in winter (Fig. 3), partly due to a reduction in sea ice and snow cover in and
272 around Hudson Bay. The mean winds from the west (Fig. 3) can transport the additional heat
273 over the adjacent ocean, where increased air temperature warms the underlying ocean via the
274 surface heat fluxes, especially near the coast. The increase in air temperature over North

275 America corresponds to the overall climate sensitivity of these three GCMs, which is relatively
276 weak, moderate and strong, in the GFDL, IPSL and HadGEM GCMs (Table 1, Fig. 3),
277 respectively, as are the increases in SST off the coast of the northeast US and southern Canada
278 in the GCMs (Fig. SM2) and the corresponding ROMS simulations (Fig. 2).

279 There are also clear differences between the downscaled simulations and the corresponding
280 GCMs which drove them. In the GFDL and IPSL experiments, the downscaled simulation
281 exhibits less warming in the Gulf Stream region compared to the GCM, while for HadGEM,
282 the ROMS simulation generally exhibits less warming over much of the domain except along
283 portions of the eastern seaboard relative to the driving GCM. Differences between the global
284 and regional SST responses to anthropogenic forcing reached 2°C in some locations.

285 The bottom temperature (BT) response in all three downscaled experiments indicates
286 warming along the entire continental shelf in both DJF and JJA (Fig. 4). They also indicate
287 enhanced warming over portions of maritime Canada, on the shelf in the Gulf of Mexico, and
288 in a narrow band along the shelf break (in the vicinity of the 200 m isobath) off the southeast
289 US coast in summer. The increase in bottom temperature in coastal regions is often greater
290 than at the surface in all three simulations. For example, the increase in SST during JJA over
291 the west Florida shelf is on the order of 2.5°C but for BT it exceeds 3.5°C in all three ROMS
292 simulation. There are also substantial differences in the detailed BT structure among the three
293 ROMS simulations, which are clearly influenced by both the large-scale forcing and small-
294 scale topographic features (compare Figs. 4 and SM3). Like SST, the strongest increase in BT
295 (> 4°C) occurs over a broad region north of Cape Hatteras in HadGEM-ROMS. At regional
296 scales, which are not resolved by the GCMs, a strong BT response occurs in the Laurentian
297 Channel that extends from the shelf break to the mouth of the Saint Lawrence River in GFDL-

298 ROMS. In contrast, the strongest increase in BT in IPSL-ROMS and HadGEM-ROMS is not
299 in the bottom of the Channel, but in shallower portions of the Gulf of Saint Lawrence and on
300 the shelf off the coast of Newfoundland and Nova Scotia.

301 In many locations along the continental shelf, the warming at the bottom is greater than
302 at the surface. If the main source of warming was generated locally through the atmosphere,
303 then the expectation is that the warming would be greatest at the surface and decrease with
304 depth. However, the source for water at depth can differ from those at the surface. Along the
305 northeast coast, much of the source waters originate (are ventilated) in the Labrador Sea/North
306 Atlantic and are transported southward at depth along the shelf (Chen et al. 2018). In all three
307 of our ROMS experiments, the warming due to climate change within or entering the northern
308 part of the domain is especially strong. Changes in temperature and/or flow can alter the heat
309 transport by coastal currents along the shelf, and thus, the change in temperature can be greater
310 at the bottom than at the surface. In addition, the ROMS simulations are much less diffusive
311 than the GCMs and thus are able to resolve coastally trapped currents, leading to enhanced
312 warming along the shelf edge compared to GCMs (Saba et al. 2016; Shin and Alexander 2019).

313

314 *b. Salinity*

315 The sea surface salinity (SSS) response in ROMS for the three forcing experiments is
316 shown for DJF and JJA in Fig. 5. The SSS values exhibit decreased salinity in the northwest
317 corner of the domain in both summer and winter. Like the ROMS simulations, the large-scale
318 salinity changes in the original GCM simulations indicate a decrease in salinity north of $\sim 40^{\circ}\text{N}$
319 (Fig. SM4), partly due to increased net surface freshwater flux into the ocean; i.e. $\Delta(\text{E-P})$ is
320 generally negative with large amplitude over the center of the subpolar gyre and the southern

321 Labrador Sea (Fig. SM5), but more regional E-P changes vary in magnitude, location and by
322 season among the three GCMs. Since the largest response in E-P and the melting of sea ice
323 primarily occur outside of the ROMS domain, the decrease in salinity off the New England
324 and Canadian coast is likely due to advection of fresher water into the region. The salinity
325 increase south of 40°N, is generally consistent with where $\Delta(E-P) > 0$.

326 Notable differences in SSS occur along the northeast US coast among the three ROMS
327 simulations and between the individual ROMS simulations and the GCMs that drove them.
328 The southward extent of enhanced freshening along the coast of North America is greatest in
329 GFDL-ROMS, where it extends to North Carolina, while it is primarily confined to Canadian
330 waters in DJF and north of New Jersey in JJA in IPSL-ROMS and HadGEM-ROMS. The
331 freshening along the northeast coast also extends further south in GFDL-ROMS than in the
332 GFDL GCM itself, while the reverse is true in the IPSL and HADGEM experiments.

333 The salinity changes in the southern portion of the domain are consistent with enhanced
334 evaporation relative to precipitation in the future climate ($\Delta(E-P) > 0$) over most of the Atlantic
335 south of ~40°N and the Gulf of Mexico in all three GCMs (Fig. SM5). However, there are
336 differences between where $\Delta(E-P)$ is large and the location and amplitude of the SSS response
337 in the ROMS simulations and the corresponding GCMs in portions of the Gulf of Mexico. This
338 difference is especially notable in the northern Gulf of Mexico in the HadGEM experiment,
339 where $\Delta E-P$ is positive and the SSS slightly increases in the GCM but decreases in HadGEM-
340 ROMS. Freshwater entering the Gulf from the Mississippi River is greatly enhanced in the
341 HadGEM GCM (Fig. SM6) resulting in SSS decreases in the future in HadGEM-ROMS
342 simulations especially in JJA (Fig. 5). Higher vertical and horizontal resolution in conjunction
343 with reduced diffusion coefficients in ROMS relative to the coarse GCMs can act to maintain

344 fine-scale features, such as river plumes. While the SSS generally increases in the other two
345 ROMS simulations in the Gulf of Mexico, the change is smaller in northern portions of the
346 basin in JJA, where changes in currents and stratification may also play a role in the detailed
347 pattern of the response.

348 The response to climate change in the bottom salinity in the three ROMS simulations is
349 shown during DJF and JJA in Fig. 6 (and in Fig. SM7 for the GCMs). They have the same
350 general structure as those at the surface over most of the domain, although the magnitude and
351 extent of the changes tend to be smaller at the bottom. However, the response is very different
352 in the Laurentian Channel where the water becomes saltier on the bottom while it is freshening
353 at the surface. The apparent change in the salinity with depth is readily apparent in GFDL-
354 ROMS, where the bottom salinity increases in the Laurentian Channel (depth > 200 m) but
355 decreases nearly everywhere else north of Nova Scotia.

356

357 *c. Cross sections*

358 The structure of the vertical temperature and salinity changes in the three ROMS
359 integrations is explored further using cross sections in the vicinity of the Laurentian
360 Channel/Gulf of Saint Lawrence, Northeast Channel/Gulf of Maine and across the northern
361 Gulf of Mexico (see Fig. 1a). Note that the first two sections follow the maximum depth in
362 their respective channels and therefore they do not follow a fixed latitude or longitude. Since
363 the cross sections are qualitatively similar in DJF and JJA, we present the annual mean values
364 for the CTRL (contours) and the RCP8.5-CTRL (shading).

365 In the Gulf of Saint Lawrence, there is a temperature minimum at ~40 m depth and a
366 vertical front near the Atlantic-Gulf boundary at ~45°N in the 30-year climatology from the

367 CTRL simulation (Fig. 7, top panels). While warming occurs throughout the Laurentian
368 Channel, the temperature departures are largest at depth in GFDL-ROMS (Fig. 7a), while the
369 maximum departures extend from near the surface to about 250 m in the other two simulations
370 (Fig. 7b,c). The maximum downscaled warming exceeds 3.5°C in the GFDL and IPSL, and
371 5°C in HadGEM. All three ROMS simulations indicate freshening of the surface layer,
372 extending to approximately 100, 75 and 50 m depth in the GFDL, HadGEM and IPSL
373 experiments, respectively, but the magnitude of the response is substantially smaller in IPSL-
374 ROMS (Fig. 7, bottom). All three simulations also have an increase in salinity at depth in the
375 Gulf of Saint Lawrence, which slopes downward from the southeast to the northwest.

376 The Gulf of Maine section (Fig. 8), includes the Northeast Channel (66°W), Georges Basin
377 (67°W) and Wilkinson Basin (69.5°W). In the CTRL, there is a strong vertical thermohaline
378 front near the entrance to the Gulf of Maine around ~65.5°W with colder and fresher water in
379 the Gulf relative to the Atlantic. The strongest warming in GFDL-ROMS is located at depths
380 below ~130 m in the open ocean (east of 65.5°W), which extends into Georges Basin through
381 the Northeast Channel (Fig. 8a, also see Shin and Alexander 2019). In the other two simulations
382 (Fig. 8 b,c), the warming occurs higher in the water column, where the temperature departures
383 exceed 5°C in HadGEM-ROMS at ~60 m depth at ~67.5°W. While salinity is enhanced in all
384 three simulations in the Atlantic, the overall response strongly differs between them (Fig. 8
385 bottom panels). The most notable difference occurs in the surface layer in the Gulf of Maine
386 where GFDL-ROMS exhibits freshening while the salinity increases in IPSL-ROMS and to a
387 lesser degree in HadGEM-ROMS. In the open ocean, the salinity increases by more than 0.4
388 PSU at depths greater than ~150 m in GFDL-ROMS, while the changes are slightly smaller
389 and occur higher in the water column in the two other simulations. Only a small amount of the

390 saltier water extends into the Gulf of Maine, likely advected through the northeast channel in
391 the GFDL-ROMS, resulting in slightly saltier water below ~200 m in Georges Basin. In IPSL-
392 ROMS, a layer with enhanced salinity penetrates eastward over the entire Gulf of Maine, with
393 a maximum at ~50 m within the climatological halocline but also with salty water penetrating
394 to the bottom of Georges Basin. HadGEM-ROMS is somewhere between the two other
395 experiments, where the increase in salinity also slopes downward into Georges Basin, with a
396 weak response above 50 m.

397 The temperature and salinity changes differ between the surface and the bottom in the
398 northern Gulf of Mexico (sections 3a&b), indicating vertical structure in the response to
399 climate change; thus, we present a zonal section along 28°N between the central coasts of
400 Florida and Texas (Fig. 9). The CTRL exhibits a steady decrease in temperature with depth
401 with a maximum gradient from around 40 to 150 m, where the thermocline is stronger and
402 shallower near the coasts. The salinity in the CTRL exhibits much less vertical structure, but
403 has a broad maximum over approximately 85°-93°W, with much fresher water near the coasts.
404 In all three ROMS simulations, the temperature change is positive over the full width and depth
405 of the Gulf of Mexico and is larger at depths between approximately 40-150 m than at the
406 surface (Fig. 9 top panels), though the warming is slightly greater and most extensive in GFDL-
407 ROMS. The response is enhanced where the thermocline intersects the west Florida Shelf at
408 ~85°W, especially in GFDL-ROMS and HadGEM-ROMS, where it reaches 5°C, in line with
409 the strong increase in bottom temperature on the west Florida Slope (Fig. 4). The respective
410 increases in salinity are relatively strong, moderate and weak in the downscaled GFDL, IPSL,
411 HadGEM simulations, respectively (Fig. 9 bottom panels). The changes are largest near the
412 Florida Coast in GFDL-ROMS and HadGEM-ROMS and near the Texas Coast in the shallow

413 climatological halocline in all three ROMS integrations. The salinity responses are also
414 enhanced across the entire basin between approximately 40 and 100 m depth in IPSL-ROMS
415 and HadGEM-ROMS; there is a slight increase at depth in GFDL-ROMS but it does not extend
416 across the basin.

417

418 *d. Density*

419 The depth dependent changes in temperature and salinity alter the density profile and thus
420 stratification. Stratification, as indicated by the density difference between 100 m depth and
421 the surface, is positive for stable stratification. The changes in stratification are shown for the
422 three ROMS simulations during DJF and JJA in Fig. 10; the separate contributions of
423 temperature and salinity to the annual mean density at the surface, 100 m and the stratification,
424 are shown in Figure SM8. With intensified surface warming in the future most of the open
425 ocean areas of the North Atlantic in all three ROMS simulations display an increase in
426 stratification particularly in summer, consistent with Capotondi et al. (2012) and Alexander et
427 al. (2018). The change in the vertical structure of salinity enhances the stratification in the
428 northern part of the domain in all three ROMS simulations, and is especially strong along the
429 northern edge of the Gulf Stream and in the Laurentian channel in the GFDL and HadGEM
430 models (Fig. SM8). The change in stability is also more complex than just a surface intensified
431 warming in the Gulf Stream region and in the Gulf of Mexico. There is a decrease in
432 stratification in the Gulf Stream near the coast and a near-neutral response as it leaves the coast
433 near Cape Hatteras and extends into the Atlantic (where it is a minimum in the CTRL) during
434 winter. Off the southeast US coast, the weakening of the Gulf Stream is greater at the surface
435 than at depth (discussed in the following section) and there is intensified warming adjacent to

436 the shelf break both of which may enhance warming at depth relative to the surface. The
437 stratification actually decreases over nearly all of the Gulf of Mexico in GFDL-ROMS and
438 IPSL-ROMS and in the center of the Gulf in HadGEM-ROMS during DJF. In the Gulf,
439 warming at 100 m depth, which is within the upper thermocline (Fig. 9), is greater than at the
440 surface, which reduces the stratification in the downscaled simulations (Fig. SM8; the
441 stratification and its decomposition in the three GCMs are shown in Figs. SM9 & SM10). The
442 stratification changes vary among the three ROMS simulations over the Gulf of Mexico during
443 JJA (Fig. 10), but all three exhibit decreased stratification in the east-central part of the basin
444 ($\sim 25^{\circ}\text{N}$, 87°W).

445

446 *e. Currents*

447 A clear result in all three ROMS simulations is the weakening of the western boundary
448 current system over the entire domain including the Yucatan, Loop, and Florida Currents and
449 the Gulf Stream in both winter and summer (Fig. 11). The three forcing GCMs also show a
450 weakening of the western boundary current system in the western North Atlantic, although the
451 reduction in current strength in the IPSL GCM (Fig. SM11) is smaller than in IPSL-ROMS.
452 The weakening of the currents is especially pronounced in the Gulf Stream, whose speed
453 decreases by more than 25% in the three ROMS simulations relative to the CTRL, as indicated
454 by a cross section of the meridional velocity at 30°N (Fig. 12). A more detailed map of the
455 annual mean surface currents off the NE US coast for the CTRL and the response to climate
456 change in three ROMS experiments are shown in Fig. 13. The response in GFDL- ROMS
457 simulation opposes the mean Gulf Stream flow in the center and northern part of the current
458 with a weak enhancement on its southern flank. This is highlighted in a meridional cross

459 section of the zonal current at 70°W (Fig. 14a) indicating a southward displacement of the
460 current where the Gulf Stream is mainly zonal. The response in IPSL-ROMS and HadGEM-
461 ROMS exhibit an anomalous anticyclonic (clockwise) gyre starting near Cape Hatteras, where
462 the current separates from the coast, to the south of Long Island (~72°W, Fig. 13c) in IPSL-
463 ROMS and Cape Cod (~65°W, Fig. 13d) in HadGEM-ROMS. This feature weakens the
464 northern core of the Gulf Stream but enhances northeasterly flows along its northern edge
465 (Figs. 11,13). The latter aspect of the response is consistent with Saba et al. (2016), who found
466 enhanced meridional flow nearshore (~36°N, 74°W) and a northward shift of the current.
467 However, the enhanced flow on the northernmost edge of the Gulf Stream remains south of
468 ~40°N and west of the Gulf of Maine in both IPSL-ROMS and HadGEM-ROMS (Figs. 11, 13,
469 14). In addition, the response in all three ROMS simulations indicates that water enters the
470 Gulf of Maine from the east along the Scotian Shelf and then flows counterclockwise around
471 the basin. This enhances the mean circulation at the surface (Fig. 13) and at depths down to
472 200 m (as can be displayed at <https://www.esrl.noaa.gov/psd/ipcc/roms/roms.html>). Thus, the
473 responses of all three ROMS simulations, especially GFDL-ROMS, differ from the findings
474 of Saba et al. (2016) who found that the warming in the Gulf of Maine at depth was due to a
475 northward shift of the Gulf Stream. There are several potential explanations for why the Gulf
476 of Maine warms without a northward shift in the Gulf Stream, as discussed in the section 4.

477 The Gulf Stream is driven by both buoyancy and wind forcing over the North Atlantic, thus
478 changes in its strength and position can be associated with AMOC and the wind driven gyre
479 circulation. The latter is classically related to the zonal integration of the wind stress curl across
480 the basin. Given that the surface winds (and thus zonally-integrated wind stress curl) are very
481 different in the three GCMs over the Atlantic Ocean (Fig. SM12), suggests that it's changes in

482 AMOC, rather than wind-driven changes in the gyre circulation, that is critical for the
483 weakening of the Gulf Stream prevalent in all of the GCM and ROMS simulations. Changes
484 in the basin-wide wind stress, however, may contribute to the positional differences in the Gulf
485 Stream among the three simulations. Regional changes in the buoyancy forcing, via surface
486 fluxes of heat and freshwater, that result in changes in the gradients of density/sea surface
487 height can also influence western boundary currents (Lowe and Gregory 2006; Suzuki and
488 Ishii 2011; Liu et al. 2015).

489

490 *f. Eddies*

491 Eddy activity is represented by the eddy kinetic energy (EKE, $0.5(u'^2 + v'^2)$), calculated
492 from the currents in the surface layer, where the departures ($'$) are obtained from pentad values
493 after subtracting a 120-day mean centered on that pentad. In the CTRL, eddies are prominent
494 in the Gulf Stream after it separates from the coast, in the Loop Current region of the Gulf of
495 Mexico, and southeast of the Yucatan Peninsula in summer (contours in Fig. 15). The general
496 pattern of the change in eddies in all three simulations is similar to those of the currents, with
497 a decrease in eddy activity in the center of the Gulf Stream region, where the maximum EKE
498 occurs in the CTRL. In GFDL-ROMS there is a decrease in EKE on the northern flank of the
499 Gulf Stream and a slight decrease on its southern edge, and these changes are slightly larger in
500 JJA than in DJF. In contrast, in IPSL-ROMS and HadGEM-ROMS there is an increase
501 (decrease) in EKE on the northern (southern) edge of the Gulf Stream in both DJF and JJA.
502 This increase in EKE occurs in a narrow band from the coast northeastward for $\sim 8^\circ$ of
503 longitude, but then becomes broader but more diffuse south of Nova Scotia ($\sim 65^\circ\text{W}$) and
504 further to the east. All three downscaled simulations show a decrease in eddy activity in the

505 vicinity of the Loop Current in DJF, with an increase (decrease) on its western (eastern) side
506 during JJA. The EKE increases in the western half of the Gulf of Mexico (west of 90°W)
507 especially during summer. Further south, the EKE differs between the simulations in the
508 Caribbean Sea, where it generally decreases in the GFDL-ROMS in winter and on the western
509 side of the sea in summer, but increases in the IPSL-ROMS and HadGEM-ROMS in both
510 seasons.

511

512 **4. Summary and Conclusions**

513 We used the regional ocean model system (ROMS) with 7 km resolution to downscale the
514 effects of climate change on the western North Atlantic and Gulf of Mexico. First, a control
515 simulation (CTRL) was conducted using observationally-based atmosphere and ocean fields
516 as boundary conditions. Then monthly mean differences (Δ s) in surface fluxes and ocean
517 conditions between 1976-2005 and 2070-2099 were obtained from three CMIP5 GCMs:
518 GFDL, IPSL, and HadGEM, and added to the CTRL. Finally, the response to anthropogenic
519 forcing was obtained from the difference between each of the three Δ -forced simulations and
520 the CTRL.

521 The climate change response in the three downscaled simulations, termed GFDL-ROMS,
522 IPSL-ROMS and HadGEM-ROMS, during winter (DJF) and summer (JJA) reflects both the
523 large-scale forcing and more regional changes resulting from mesoscale dynamics and
524 interaction with coastal features. All three simulations show strong increases in SSTs over most
525 of the domain, except in the vicinity of the US mid-Atlantic coast during DJF, where weaker
526 warming is associated with a reduction in strength of the Gulf Stream. Eddies also effect
527 temperatures in the western North Atlantic (Griffies et al., 2015; Saenko 2015; Treguier et al.

528 2017) and likely influence the SST changes that occur in our experiments. The difference in
529 the SST response between the Gulf Stream and the surrounding ocean decreases in summer as
530 a shallow mixed layer forms and the heating from the atmosphere is distributed over a thinner
531 layer.

532 Consistent with previous studies, the weakening of the Gulf Stream is likely caused by a
533 reduction in high latitude buoyancy and a slowing of AMOC, as opposed to wind-driven changes
534 in the gyre circulations, since the wind stress changes across the Atlantic are very different in the
535 three GCMs used to drive ROMS. Regional differences in surface fluxes, which alter the gradients
536 of density of the upper ocean may also influence western boundary currents (Lowe and Gregory
537 2006; Suzuki and Ishii 2011; Liu et al. 2015).

538 The large-scale forcing can also result in substantial differences among the three ROMS
539 simulations. The warming of SSTs north of the Gulf Stream increases in magnitude and extent
540 from GFDL-ROMS to IPSL-ROMS to HadGEM-ROMS, with the response in HadGEM-
541 ROMS being approximately 1°-2.5°C stronger than in GFDL north of ~40°N. While the
542 warming in HadGEM-ROMS tends to be largest at or near the surface, the maximum warming
543 is often at depth in GFDL-ROMS.

544 The large-scale differences in the temperature and salinity response as a function of depth
545 strongly influences the changes in nearshore regions, which are well resolved in the ROMS
546 simulations but not in the GCMs. For example, the strongest warming in GFDL-ROMS enters
547 the gulfs of Saint Lawrence and Maine near the bottom of deep channels, while the maximum
548 warming occurs higher in the water column in the other two simulations resulting in greater
549 warming along the banks of these two gulfs. The vertical structure of the salinity response is
550 also markedly different in the three downscaled simulations in some regions. For example, the

551 salinity decreases in the surface layer in the Gulf of Maine and increases at depth in GFDL-
552 ROMS simulation, while the salinity increase extends over the depth of the Gulf in the other
553 two simulations.

554 Differences in the downscaled simulations also arise in the Gulf of Mexico, where the
555 largest increase in temperature occurs within the thermocline during winter in GFDL-ROMS
556 and to a lesser degree in IPSL-ROMS, but occurs near the surface in HadGEM-ROMS. As a
557 result, the stratification, as given by the difference in density between the surface and 100 m,
558 actually decreases over the most of the Gulf of Mexico in GFDL-ROMS and IPSL-ROMS in
559 winter, opposite to the general increase in stratification that is projected to occur over most of
560 the world's oceans. The response is especially strong where thermocline abuts the shelf,
561 creating exceptionally warm ($> 4^{\circ}\text{C}$) bottom temperatures on the West Florida slope and shelf.
562 Other processes also influence the response in the Gulf of Mexico. For example, changes in
563 runoff from the Mississippi River, which greatly increases in HadGEM-ROMS, results in a
564 decrease in salinity in the northern Gulf. In addition, enhanced eddy activity occurs on the
565 western side of the Loop Current and extends across the western portion of the basin in all
566 three downscaled simulations, suggesting that more eddies may shed from the Loop Current
567 and propagate westward in the future. Thus, a wide array of both atmosphere and ocean
568 processes may influence how climate change unfolds in the Gulf of Mexico.

569 In addition to the overall reduction in the strength of the western boundary current system,
570 including the Yucatan, Loop and Florida currents as well as the Gulf Stream, the fine resolution
571 in the ROMS simulations allows for regional ocean circulation changes. The Gulf Stream
572 exhibits a southward shift in GFDL-ROMS and a slight northward shift in the other two ROMS
573 simulations. The northward shift is part of an elongated anticyclonic gyre circulation which

574 reaches approximately 72°W and 65°W in the IPSL-ROMS and HadGEM-ROMS,
575 respectively. A commensurate meridional shift occurs in the eddy kinetic energy. However, all
576 three model simulations suggest that the changes in the Gulf Stream remain well to the south
577 of New England and that climate change enhances the present-day circulation, with water
578 entering the Gulf of Maine from the east and then flowing counterclockwise around the basin
579 (also see Shin and Alexander 2019). In contrast, using a high-resolution global model, Saba et
580 al. (2016) found that enhanced warming at depth in the Gulf of Maine was due to a northward
581 shift of the Gulf Stream.

582 Since a northward shift of the Gulf Stream does not appear to directly cause the enhanced
583 warming in the Gulf of Maine, what processes could be involved in the very strong temperature
584 response there? The enhanced warming in the gulfs of Maine and Saint Lawrence may result
585 from a number of processes including:

- 586 • Very strong warming of the atmosphere over eastern Canada ($> 8^{\circ}\text{C}$) that is transported
587 over the Atlantic due to advection by westerly winds (see Fig. 3), heating the ocean via
588 changes in the surface fluxes. This atmospheric related heating may partly explain the
589 warming adjacent to the northeast US and Atlantic Canadian provinces as indicated by
590 present day ocean heat budget analyses (Chen et al. 2015, 2016) and by climate
591 equilibrium studies in which greenhouse gasses are increased (often doubled) in a
592 global atmospheric model that is coupled to an ocean model without currents (e.g.
593 Danabasoglu and Gent 2009; Dommenges 2012). The increase in surface air
594 temperatures over North America is modest, intermediate, and strong in the GFDL,
595 IPSL and HadGEM models respectively, which corresponds to the magnitude of the

596 warming of SSTs off the coast of New England and Canada's Atlantic provinces in
597 both the GCMs and the corresponding ROMS simulations.

598 • With polar amplification of the climate change signal, the Arctic Ocean and Labrador
599 Sea are projected to undergo very strong warming by the end of the 21st century,
600 especially in regions where the ice has retreated from. This much warmer water relative
601 to today's climate can then be advected by the east Greenland current and Labrador
602 currents from Newfoundland to the northeast US coast.

603 • The reduction in AMOC enhances the absorption of heat from the atmosphere at high
604 latitudes (Rugenstein et al. 2013), which can subsequently be advected by the Labrador
605 current to the NE US Shelf as described above.

606 • CMIP5 models, including the three used here, indicate a small region of very strong
607 warming in the vicinity of ~44°N-45°W, southeast of Newfoundland, associated with
608 more northward directed currents in the future (Fig SM13). While most of the changes
609 in currents are directed towards the southwest, these changes in temperature and
610 currents appear to be linked to the overall reduction in AMOC (Cheng et al. 2013,
611 Winton et al. 2013; Buckley and Marshall 2016). The very warm water can
612 subsequently be advected into the Gulf of Maine as indicated by backward trajectories
613 derived from the GFDL-ROMS simulation (Shin and Alexander 2019) and analyses of
614 observations and a model simulation of the past decade (Brickman et al. 2018).

615 • Ocean eddies in the vicinity of the Gulf Stream may transport warm salty water towards
616 the NE US shelf, especially in the IPSL-ROMS and HadGEM- ROMS simulations,
617 where there are semi-permanent eddies south of Nova Scotia (Fig. 12) and an increase

618 in transient eddy activity on the northern flank of the Gulf Stream/North Atlantic
619 Current (Fig 14).

620 Differences in salinity also occur along the northeast US coast among the three ROMS
621 simulations and between the global and downscaled simulations. The southward extent of
622 enhanced freshening is greatest in GFDL-ROMS, where it extends to Cape Hatteras off North
623 Carolina at both the surface and on the bottom, while it is primarily confined to Canadian
624 waters in IPSL-ROMS and HadGEM-ROMS during DJF (Figs. 5 and 6). In addition, the
625 freshening along the northeast coast extends further south in GFDL-ROMS than in the
626 corresponding GCM simulation. The salinity response may reflect changes in salinity
627 advection due both to changes in the currents and changes in the water properties, i.e. the water
628 becoming fresher. The southward shift in the Gulf Stream, which only occurs in the GFDL-
629 ROMS simulation, enables currents to transport relatively fresh water originating in the
630 Labrador Sea/Subarctic Gyre all the way to where the Gulf Stream separates from the coast at
631 Cape Hatteras. In addition, the large-scale forcing causes strong freshening in the northeast
632 part of the domain, especially in the GFDL and HadGEM models. The decrease in salinity is
633 maintained in an upper layer adjacent to the northeast coast in the GFDL-ROMS off the New
634 England coast (Fig. 8). A cross section of the zonal current and the salinity response along
635 70°W in the three ROMS simulations, highlights both the stronger westward (negative) current
636 change and the enhanced freshening in the GFDL-ROMS model relative to the other two
637 downscaled simulations (Fig. 16). In contrast, the response exhibits a narrow band of eastward
638 currents and increased salinity in the vicinity of 39.7°N, suggesting eastward salinity advection
639 south of Cape Cod in the IPSL-ROMS and HadGEM-ROMS simulations. While freshening
640 also occurs off the New England coast in the GFDL GCM (Fig. SM4), the current changes are

641 much weaker and the change in salinity confined closer to the coast than in the corresponding
642 ROMS integrations (Fig. 16). Thus, the surface layer freshening can be maintained and
643 advected southeastward by stronger coastal currents in the GFDL-ROMS simulation relative
644 to the more diffusive and sluggish GFDL GCM. In addition, the freshwater flux at the surface
645 (P-E) increases as a result of climate change just off the east coast of the mid-Atlantic states in
646 summer in the GFDL and HadGEM GCMs (Fig. SM5), which contributes to the freshening
647 that occurs in JJA in the corresponding ROMS simulations (Fig. 4). Other processes, such as
648 river runoff, stratification, eddy mixing, etc., could also influence the detailed structure of the
649 salinity changes.

650 While there is a strong link between changes in mean currents and eddy activity, e.g. as
651 illustrated by the corresponding meridional shift in the Gulf Stream and EKE in each ROMS
652 integration, there is not necessarily a one-to-one relationship between them. For example, the
653 Yucatan current weakens while the EKE increases in the northwestern Caribbean Sea during
654 DJF in HadGEM-ROMS (cf. Fig. 11c and Fig. 15c). Eddies are generated and dissipated by a
655 wide range of processes, including interactions with mean currents and topography, wind and
656 buoyancy forcing, and baroclinic, barotropic and symmetric instabilities (e.g. McWilliams
657 2008). These processes vary with the seasonal cycle and location, including in the Gulf Stream
658 region (e.g. Kang and Curchitser 2015 and Kang et al. 2016) and the Gulf of Mexico (Oey et
659 al. 2005), where eddy activity can be strong during. Anticyclonic eddies are generated in the
660 Loop Current and propagate westward across the Gulf of Mexico, where eddy shedding
661 preferentially occurs in summer and winter relative to spring and fall (Chang and Oey 2012;
662 Hall and Leben 2016). In our three experiments, the EKE is strongly enhanced on the western
663 and northern flanks of the Loop Current in summer but not in winter and the increase in EKE

664 is somewhat stronger in JJA than DJF across the western portion of the Gulf of Mexico. One
665 potential source of these differences may lie in the seasonal change in the winds over the
666 Caribbean Sea and Gulf of Mexico (Fig. SM12), which influence the northward extent of the
667 Loop Current and eddy shedding (Chang and Oey 2012). The links between the changes in
668 winds, AMOC/western boundary currents, and eddies are multi-faceted, and thus warrant
669 further study.

670 The differences between the three ROMS simulations, and between the ROMS simulations
671 and the high-resolution global model simulation analyzed by Saba et al. 2016, indicate that
672 while high resolution allows for better representation of the large-scale and regional
673 circulation, it doesn't guarantee the same climate change response, which depends on a wide
674 range of factors. These findings suggest that even when using dynamically downscaled
675 regional ocean models or high-resolution global models to investigate the oceanic response to
676 climate change, one should use an ensemble of global models with multiple realizations from
677 each model to capture structural uncertainty in the models and the range of potential outcomes
678 that result.

679
680 **Acknowledgements**

681 We thank Michael Jacox, the three anonymous reviewers and Oleg Saenko – the editor, for
682 their constructive comments. This study is supported by grants from the NOAA Coastal and
683 Climate Applications (COCA) program #NA-15OAR4310133 and #NA-17OAR4310268.
684 Contributing support for this work was provided by the NOAA Integrated Ecosystem
685 Assessment (IEA) Program. This manuscript is IEA Contribution Number 2019_7.

686

687

688

689 **References**

690 Alexander M.A., J.D. Scott, K.D. Friedland, K.E. Mills, J.A. Nye, A.J. Pershing, and A.C.
691 Thomas, 2018: Projected sea surface temperatures over the 21st century: Changes in the
692 mean, variability and extremes for large marine ecosystem regions of Northern
693 Oceans. *Elementa: Science of the Anthropocene*, **6(1):9**, DOI:
694 <http://doi.org/10.1525/elementa.191>

695

696 Auad, G., A. Miller, E. Di Lorenzo E. 2006: Long-term forecast of oceanic conditions off
697 California and their biological implications. *J. Geophys. Res.-Oceans.*,
698 **111**, 10.1029/2005jc003219

699

700 Belkin, I.M., 2009 Rapid warming of Large Marine Ecosystems. *Prog. Oceanogr.*, **81(1–4)**:
701 207–213. DOI: <https://doi.org/10.1016/j.pocean.2009.04.011>

702

703 Boyer, T. P., Levitus, S., Antonov, J. I., Locarnini, R. A., and H. E. Garcia, 2005: Linear trends
704 in salinity for the World Ocean, 1955–1998. *Geophys. Res. Lett.* **32**,
705 doi:10.1029/2004GL021791.

706

707 Brickman, D., D. Hebert and Z. Wang, 2018: Mechanism for the recent ocean warming events
708 on the Scotian Shelf of eastern Canada. *Cont. Shelf Res.*, **156**, 11-24.
709 <https://doi.org/10.1016/j.csr.2018.01.001>.

710

711 Bryan, F. O., M. W. Hecht, and R. D. Smith, 2007: Resolution convergence and sensitivity
712 studies with North Atlantic circulation models. Part I: The western boundary current
713 system, *Ocean Model.*, **16**, 141–159, doi:10.1016/j.ocemod.2006.08.005.
714

715 Buckley, M. W., and J. Marshall, 2016: Observations, inferences, and mechanisms of Atlantic
716 Meridional Overturning Circulation variability: A review. *Rev. Geophys.*, **54**, 5–63,
717 doi:10.1002/2015RG000493.
718

719 Capotondi, A., M. A. Alexander, N. A. Bond, E. N. Curchitser, and J. D. Scott, 2012: Enhanced
720 upper ocean stratification with climate change in the CMIP3 models, *J. Geophys. Res.*, **117**,
721 C04031, doi:10.1029/2011JC007409.
722

723 Carton, J. A., and B. S. Giese, 2008: A reanalysis of ocean climate using Simple Ocean Data
724 Assimilation (SODA). *Mon. Wea. Rev.*, **136**, 2999–3017, doi:
725 <https://doi.org/10.1175/2007MWR1978.1>.
726

727 Caesar, L., S. Rahmstorf, A. Robinson, G. Feulner, and V. Saba, 2018: Observed fingerprint
728 of a weakening Atlantic Ocean overturning circulation. *Nat. Clim. Change*, **556**, 191-196,
729 doi: 10.1038/s41586-018-0006-5.
730

731 Chang, Y. -L., and L.-Y. Oey, 2012: Why does the Loop Current tend to shed more eddies in
732 summer and winter? *J. Geophys. Res.: Oceans*, **39**, L05605, doi:10.1029/2011GL050773.
733

734 Chen K., G. G. Gawarkiewicz, S. J. Lentz S. J., and J. M. Bane, 2014: Diagnosing the
735 warming of the Northeastern US Coastal Ocean in 2012: A linkage between the
736 atmospheric jet stream variability and ocean response. *J. Geophys. Res.: Oceans*, **119**, 218–
737 227. <https://doi.org/10.1002/2013JC009393>
738
739
740 Chen, K., G. Gawarkiewicz, Y.-O. Kwon, and W. G. Zhang, 2015: Role of atmospheric forcing
741 versus ocean advection during the anomalous warming on the Northeast U.S. shelf in
742 2012, *J. Geophys. Res.*, **120**, 4324–4339, doi:10.1002/2014JC010547.
743
744 Chen, K., Y.-O. Kwon, and G. Gawarkiewicz, 2016: Interannual Variability of Winter-Spring
745 Temperature in the Middle Atlantic Bight: Relative Contributions of Atmospheric and
746 Oceanic Processes. *J. Geophys. Res.: Oceans*, **121**, 4209–4227. 10.1002/2016JC011646.
747
748 Chen, Z., E. Curchitser, R. Chant, and D. Kang, , 2018: Seasonal variability of the cold pool
749 over the Mid-Atlantic Bight continental shelf. *J. Geophys. Res.: Oceans*, **123**, 8203–8226.
750 <https://doi.org/10.1029/2018JC014148>.
751
752 Cheng, W., J.C. Chiang, and D. Zhang, 2013: Atlantic Meridional Overturning Circulation
753 (AMOC) in CMIP5 Models: RCP and Historical Simulations. *J. Climate*, **26**, 7187–
754 7197, <https://doi.org/10.1175/JCLI-D-12-00496.1>
755

756 Collins, M., R. Knutti, J. Arblaster, J.-L. Dufresne, T. Fichefet, P. Friedlingstein, X. Gao, W.
757 J. Gutowski, T. Johns, G. Krinner, M. Shongwe, C. Tebaldi, A.J. Weaver and M. Wehner,
758 2013: Long-term Climate Change: Projections, Commitments and Irreversibility. In:
759 Climate Change 2013: The Physical Science Basis. Contribution of Working Group I to
760 the Fifth Assessment Report of the Intergovernmental Panel on Climate Change [Stocker,
761 T.F., D. Qin, G.-K. Plattner, M. Tignor, S.K. Allen, J. Boschung, A. Nauels, Y. Xia, V.
762 Bex and P.M. Midgley (eds.)]. Cambridge University Press, Cambridge, United Kingdom
763 and New York, NY, USA.

764

765 Coumou, D., G. Di Capua, S. Vavrus, L. Wang, S. Wang, 2018: The influence of Arctic
766 amplification on mid-latitude summer circulation. *Nat. Commun.*, **9**, Article number: 2959.
767 10.1038/s41467-018-05256-8

768

769 Dai., A., T. Qian, K. E. Trenberth , and J. D. Milliman, 2009: Changes in continental freshwater
770 discharge from 1948-2004, *J. Climate*, **22**, 2773-2792.

771

772 Danabasoglu, G., 2008: On Multidecadal Variability of the Atlantic Meridional Overturning
773 Circulation in the Community Climate System Model Version 3. *J. Climate*, **21**, 5524–
774 5544, <https://doi.org/10.1175/2008JCLI2019.1>

775

776 Danabasoglu, G. and P. R. Gent, 2009: Equilibrium Climate Sensitivity: Is It Accurate to Use
777 a Slab Ocean Model?. *J. Climate*, **22**, 2494–2499,
778 <https://doi.org/10.1175/2008JCLI2596.1>

779

780 Deser, C., A. S. Phillips, M. A. Alexander, and B. V. Smoliak, 2014: Projecting North
781 American Climate over the next 50 years: Uncertainty due to internal variability. *J.*
782 *Climate*, **27**, 2271-2296, doi: 10.1175/JCLI-D-13-00451.1.

783

784 Dommenges, D., 2012: Comments on “The Relationship between Land–Ocean Surface
785 Temperature Contrast and Radiative Forcing”, *J. Climate*, **25**, 3437–3440.

786

787 Drijfhout, S., van Oldenborgh, G. J. and Cimadoribus, A., 2012: Is a decline of AMOC causing
788 the warming hole above the North Atlantic in observed and modeled warming patterns? *J.*
789 *Climate*, **25**, 8373–8379. <https://doi.org/10.1175/JCLI-D-12-00490.1>

790

791 Flato, G., J. and Coauthors, 2013: Evaluation of Climate Models. In: *Climate Change 2013:*
792 *The Physical Science Basis. Contribution of Working Group I to the Fifth Assessment*
793 *Report of the Intergovernmental Panel on Climate Change* [Stocker, T.F., D. Qin, G.-K.
794 Plattner, M. Tignor, S.K. Allen, J. Boschung, A. Nauels, Y. Xia, V. Bex and P.M. Midgley
795 (eds.)]. Cambridge University Press, Cambridge, United Kingdom and New York, NY,
796 USA.

797

798 Gleckler, P. J., K. E. Taylor, and C. Doutriaux, 2008: Performance metrics for global climate
799 models. *J. Geophys. Res.*, **113**, D06104. doi:10.1029/2007JD008972.

800

801 Gregory, J. M., and Coauthors, 2005): A model intercomparison of changes in the Atlantic
802 thermohaline circulation in response to increasing atmospheric CO₂ concentration,
803 *Geophys. Res. Lett.*, **32**, L12703, doi:10.1029/2005GL023209.

804

805 Griffies, S. M., and Coauthors, 2015: Impacts on ocean heat from transient mesoscale eddies
806 in a hierarchy of climate models. *J. Climate*, **28**, 952–977, [https://doi.org/10.1175/JCLI-](https://doi.org/10.1175/JCLI-D-14-00353.1)
807 [D-14-00353.1](https://doi.org/10.1175/JCLI-D-14-00353.1).

808

809 Hall, C. A., and R. R. Leben, 2016: Observational evidence of seasonality in the timing of loop
810 current eddy separation. *Dyn. Atmos. Oceans.*, **76**, 240-267.
811 <https://doi.org/10.1016/j.dynatmoce.2016.06.002>

812

813 Hare, J. A., and Coauthors, 2012: Cusk (*Brosme brosme*) and climate change: assessing the
814 threat to a candidate marine fish species under the U.S. Endangered Species Act. *ICES*
815 *Journal of Marine Science*, **69**, 1753-1768.

816

817 Hermann, A. J., and Coauthors. 2016. Projected future biophysical states of the Bering Sea.
818 *Deep-Sea Res. II*, **134**, 30-47, <http://dx.doi.org/10.1016/j.dsr2.2015.11.001>.

819

820 Heuzé, C., 2017: North Atlantic deep water formation and AMOC in CMIP5 models. *Ocean*
821 *Science*. **13**, 609-622. [10.5194/os-13-609-2017](https://doi.org/10.5194/os-13-609-2017).

822

823 Jun, M., R. Knutti, and D. W. Nychka, 2008: Spatial analysis to quantify numerical model
824 bias and dependence: How many climate models are there? *J. Amer. Statistical*
825 *Association Applications and Case Studies*, **103** (483), 934-947 doi:
826 10.1198/016214507000001265.

827

828 Kang, D., and E. N. Curchitser, 2013: Gulf Stream eddy characteristics in a high-resolution
829 ocean model. *J. Geophys. Res. Oceans*, **118**, 4474–4487,
830 doi:<https://doi.org/10.1002/jgrc.20318>.

831

832 Kang, D. and E.N. Curchitser, 2015: Energetics of Eddy–Mean Flow Interactions in the Gulf
833 Stream Region. *J. Phys. Oceanogr.*, **45**, 1103–1120, [https://doi.org/10.1175/JPO-D-14-](https://doi.org/10.1175/JPO-D-14-0200.1)
834 [0200.1](https://doi.org/10.1175/JPO-D-14-0200.1)

835

836 Kang, D., E. N. Curchitser, and A. Rosati, 2016: Seasonal Variability of the Gulf Stream
837 Kinetic Energy. *J. Phys. Oceanogr.*, **46**, 1189–1207, [https://doi.org/10.1175/JPO-D-15-](https://doi.org/10.1175/JPO-D-15-0235.1)
838 [0235.1](https://doi.org/10.1175/JPO-D-15-0235.1)

839

840 Karspeck, A. R., and Coauthors 2017: Comparison of the Atlantic meridional overturning
841 circulation between 1960 and 2007 in six ocean reanalysis products. *Clim. Dyn.* **49**: 957.
842 <https://doi.org/10.1007/s00382-015-2787-7>.

843

844 Knutson, T. R., F. Zeng, and A. T. Wittenberg, 2013: Multimodel assessment of regional
845 surface temperature trends: CMIP3 and CMIP5 twentieth-century Simulations. *J.*
846 *Climate*, **26**(22): 8709–8743. DOI: <https://doi.org/10.1175/JCLI-D-12-00567.1> K
847

848 Knutti, R., C. Baumberger, and G. H. Hadorn, 2019: Uncertainty Quantification Using
849 Multiple Models—Prospects and Challenges. In: Beisbart C., Saam N. (eds) Computer
850 SimulationValidation. Simulation Foundations, Methods and Applications. Springer,
851 Cham. https://doi.org/10.1007/978-3-319-70766-2_34
852

Large, W. G., and S. G. Yeager, 2009: The global climatology of an interannually varying air–
sea flux data set. *Climate Dyn.*, **33**, 341–364, <https://doi.org/10.1007/s00382-008-0441-3>.

853 Lima, F. P. and Wethey, D. S., 2012: Three decades of high-resolution coastal sea surface
854 temperatures reveal more than warming. *Nat. Commun.*, 3:704 doi: 10.1038/ncomms1713.
855

856 Liu, Y., S.-K. Lee, B. A. Muhling, J. T. Lamkin, and D. B. Enfield, 2012: Significant reduction
857 of the Loop Current in the 21st century and its impact on the Gulf of Mexico, *J. Geophys.*
858 *Res.*, **117**, C05039, doi:10.1029/2011JC007555.
859

860 Liu Y., S.-K. Lee, D. B. Enfield, B. A. Muhling, J. T. Lamkin, F. E. Muller-Karger, M. A.
861 Roffer, 2015: Potential impact of climate change on the Intra-Americas Sea: Part-1. A
862 dynamic downscaling of the CMIP5 model projections. *J. Mar. Sys.*, **148**, 56-69, ISSN
863 0924-7963, <https://doi.org/10.1016/j.jmarsys.2015.01.007>.

864

865 Liu, Z.-J., S. Minobe, Y. N. Sasaki, and M. Terada, 2016: Dynamical downscaling of future
866 sea level change in the western North Pacific using ROMS. *J. Oceanogr.*, **72**,
867 10.1007/s10872-016-0390-0.

868

869 Lowe, J. A., and J. M. Gregory, 2006: Understanding projections of sea level rise in a Hadley
870 Centre coupled climate model, *J. Geophys. Res.*, **111**, C11014,
871 doi:10.1029/2005JC003421.

872

873 McWilliams, J. C., 2008: The Nature and Consequences of Oceanic Eddies. In Ocean
874 Modeling in an Eddy Regime, Editors: M. W. Hecht and H. Hasumi. *Amer. Geophys.*
875 *Union, Monogr. Series*, **177**, 5-15, <https://doi.org/10.1029/177GM03>.

876

877 Oey, L-Y., T. Ezer, and H-C. Lee, 2005: Loop Current, rings and related circulation in the
878 Gulf of Mexico: A review of numerical models and future challenges. In: *Circulation in*
879 *the Gulf of Mexico: Observations and Models, Geophys. Monogr.*, **161**, Amer. Geophys.
880 Union, 32–56.

881

882 Overland, J.E., M. Wang, N.A. Bond, J.E. Walsh, V.M. Kattsov, and W.L. Chapman, 2011:
883 Considerations in the selection of global climate models for regional climate projections:
884 The Arctic as a case study. *J. Climate*, **24**, 1583-
885 1597, <https://doi.org/10.1175/2010JCLI3462.1>

886

887 Pauly, D., and D. Zeller, editors (2016) *Global atlas of marine fisheries: A critical appraisal*
888 *of catches and ecosystem impacts*. Washington, DC: Island Press, 486 p.
889

890 Pedersen, R. A., I. Cvijanovic, P. L. Langen, and B. M. Vinther, 2016: The Impact of Regional
891 Arctic Sea Ice Loss on Atmospheric Circulation and the NAO. *J. Climate*, **29**, 889–
892 902, <https://doi.org/10.1175/JCLI-D-15-0315.1>
893

894 Pershing, A. J., and Coauthors, 2015: Slow Adaptation in the Face of Rapid Warming Leads
895 to the Collapse of Atlantic Cod in the Gulf of Maine. *Science*, 10.1126/science.aac9819.
896

897 Rugenstein, M. A., M. Winton, R. J. Stouffer, S. M. Griffies, and R. Hallberg, 2013: Northern
898 High-Latitude Heat Budget Decomposition and Transient Warming. *J. Climate*, **26**,609–
899 621, <https://doi.org/10.1175/JCLI-D-11-00695.1>
900

901 Saba, V. S., and Coauthors, 2016: Enhanced warming of the Northwest Atlantic Ocean under
902 climate change. *J. Geophys. Res. Oceans*, **121**, 118-132, doi:10.1002/2015JC011346.
903

904 Saenko, O.A., 2015: Strong eddy compensation for the Gulf Stream heat transport, *Geophys.*
905 *Res. Lett.*, **42**, 10739-10744, doi:<https://doi.org/10.1002/2015GL066111>.
906

907 Sanderson, B. M., R. Knutti, and P. Caldwell, 2015: Addressing Interdependency in a
908 Multimodel Ensemble by Interpolation of Model Properties. *J. Climate*, **28**, 5150–5170,
909 <https://doi.org/10.1175/JCLI-D-14-00361.1>

910

911 Shchepetkin, A. F., and J. C. McWilliams, 2003: A method for computing horizontal pressure-
912 gradient force in an oceanic model with a nonaligned vertical coordinate, *J. Geophys.*
913 *Res.*, **108**(C3), 3090, doi:10.1029/2001JC001047.

914

915 Shchepetkin, A. F., and J. C. McWilliams, 2005: The Regional Oceanic Modeling System
916 (ROMS): A split-explicit, free-surface, topography-following-coordinate oceanic
917 model, *Ocean Model.*, **9**, 347–404.

918

919 Shearman, R. K. and S. J. Lentz, 2010: Long-Term Sea Surface Temperature Variability along
920 the U.S. East Coast. *J. Phys. Oceanogr.*, **40**, 1004–
921 1017, <https://doi.org/10.1175/2009JPO4300.1>

922

923 Shin, S.-I. and M. A. Alexander, 2019: Dynamical downscaling of future hydrographic
924 changes over the northwest Atlantic Ocean. *J. Climate*. Submitted. Available at:
925

926 Sun, L., M. Alexander, and C. Deser, 2018: Evolution of the Global Coupled Climate Response
927 to Arctic Sea Ice Loss during 1990-2090 and Its Contribution to Climate Change. *J.*
928 *Climate*, **31**, 7823-7843, <https://doi.org/10.1175/JCLI-D-18-0134.1>

929

930 Suzuki T., and M. Ishii, 2011: Regional distribution of sea level changes resulting from
931 enhanced greenhouse warming in the Model for Interdisciplinary Research on Climate
932 version 3.2. *Geophys Res Lett.*, **38**(L02601). doi:10.1029/2010GL045693.

933

934 Treguier, A. M., C. Lique, J. Deshayes, and J. M. Molines, 2017: The North Atlantic Eddy
935 Heat Transport and Its Relation with the Vertical Tilting of the Gulf Stream Axis. *J. Phys.*
936 *Oceanogr.*, **47**, 1281–1289, <https://doi.org/10.1175/JPO-D-16-0172.1>

937

938 van Hooidonk, R.V., J. A. Maynard, Y. Liu, S.-K. Lee, 2015: Downscaled projections of
939 Caribbean coral bleaching that can inform conservation planning. *Global Change*
940 *Biology*, **21**, 3389–3401, doi: 10.1111/gcb.12901.

941

942 Winton, M., S.M. Griffies, B.L. Samuels, J.L. Sarmiento, and T. L.
943 Frölicher, 2013: Connecting Changing Ocean Circulation with Changing Climate. *J.*
944 *Climate*, **26**, 2268–2278, <https://doi.org/10.1175/JCLI-D-12-00296.1>

945

946 Winton, M., W. G. Anderson, T. L. Delworth, S. M. Griffies, W. J. Hurlin, and A. Rosati,
947 2014: Has coarse ocean resolution biased simulations of transient climate sensitivity?,
948 *Geophys. Res. Lett.*, **41**, 8522–8529, doi:10.1002/2014GL061523.

949

950 Wu, L., and Coauthors, 2012: Enhanced warming over the global subtropical western boundary
951 currents. *Nat. Climate Change*. **2**, 161–166. DOI: 10.1038/NCLIMATE1353.

952

953 Xiu, P., F. Chai, E. N. Curchitser, and F. S. Castruccio, 2018: Future changes in coastal
954 upwelling ecosystems with global warming: The case of the California Current System.
955 *Sci. Rep.*, **8**, article number 2866, 10.1038/s41598-018-21247-7.

956

957 Table 1. The three global climate models (GCMs) used to compute the delta (Δ) values, the
 958 mean difference between the periods (2070-2099) and (1976-2005), to incorporate the large-
 959 scale climate change forcing. The transient climate response, the change in global and annual
 960 mean surface temperature from an experiment in which the CO₂ concentration is increased by
 961 1% yr⁻¹, and calculated using the difference between the start of the experiment and a 20-year
 962 period centered on the time of CO₂ doubling (Flato et al. 2013). The AMOC values (in Sv)
 963 are given by the maximum overturning stream function value in the Atlantic. The Transient
 964 Climate Response and AMOC are indicated as weak, moderate and strong relative to the large
 965 set of CMIP5 models (Flato et al. 2013; Cheng et al. 2013; Collins et al. 2013; Heuzé 2017).
 966

Modeling Center	Model	Atmosphere Resolution	Ocean Resolution	Transient Climate Response	AMOC Strength 1976-2005	ΔAMOC Strength
NOAA Geophysical Fluid Dynamics Laboratory (GFDL) USA	ESM2M	2° lat x 2.5° lon; 24 levels	~1° lat x 1° lon; Meridional resolution increases from 30° N/S to 1/3° on the equator; tripolar grid > 65°N; 50 levels	1.3 Weak	17.9 Sv Moderate	-6.9 Sv strong
Institut Pierre-Simon Laplace (IPSL) France	CM5A-MR	1.25° lat x 2.5° lon; 39 levels	~2° lat x 2° lon; meridional resolution increases to 1/2° on the equator; 31 levels	2.0 Moderate	12.2 Weak	-3.9 Weak
Met Office Hadley Center (Had) UK	HadGE M2-CC	1.875° lat x 1.25° lon; 38 levels	~1° lat x 1° lon Increases from 30° N/S to 1/3° on the equator; 40 levels	2.5 Strong	16.8 Moderate	-4.4 Weak-to-Moderate

967

968

969

970 **Figure Captions**

971 Fig. 1. ROMS domain with (a) bathymetry (shaded, 25 m interval) at 1.85 km resolution. White
972 lines/transects depict the locations of cross-sections shown for the Laurentian Channel (Fig.
973 7), Gulf of Maine (Fig. 8), 28°N in the Gulf of Mexico (Fig. 9), 30°N east of Florida (Fig. 12),
974 and 70°W south of Cape Cod (Figs. 14 and 16). (b) Annual mean surface currents (shaded,
975 interval 10 cm s⁻¹, vector scale top of right panel) from the ROMS control (CTRL) experiment.
976

977 Fig. 2. SST in the CTRL (contours, interval 2 °C) and the SST response to climate change
978 (RCP8.5 – CTRL, shaded, interval 0.5 °C) during DJF (top row) and JJA (bottom row) in
979 ROMS driven by three GCMs: (a) (d) GFDL-ROMS, (b) (e) IPSL-ROMS, and (c) (f)
980 HadGEM-ROMS. The surface and boundary conditions for the CTRL are obtained from
981 reanalysis during 1976-2005 (historical period), with additional forcing added to the CTRL
982 that is derived from the mean difference between 2070-2099 and 1976-2005 in the three
983 RCP8.5 experiments.
984

985 Fig. 3. Surface air temperature change (RCP8.5 – historical period, shaded 1.0 °C interval) and
986 the surface winds in the RCP8.5 simulations from 2070-2099 (vectors, scale bottom right)
987 during DJF (top) and JJA (bottom) in the (a) (d) GFDL (b) (e) IPSL, and (c) (f) HadGEM
988 GCMs. This figure highlights how enhanced warming over North America, especially over
989 Canada in winter, could be advected by the winds warming the coastal ocean in the future.
990

991 Fig. 4. Bottom temperature response (RCP8.5 – CTRL, shaded, interval 0.5 °C) during DJF
992 (top row) and JJA (bottom row) in (a) (d) GFDL-ROMS, (b) (e) IPSL-ROMS, and (c) (f)
993 HadGEM-ROMS. The 200m isobath, representing the shelf break, is indicated by the black
994 curve.
995

996 Fig. 5. Sea surface salinity (SSS) response (RCP8.5 – CTRL, shaded, interval 0.1 PSU) during
997 DJF (top row) and JJA (bottom row) in (a) (d) GFDL-ROMS, (b) (e) IPSL-ROMS, and (c) (f)
998 HadGEM -ROMS.
999

1000 Fig. 6. Bottom salinity response (RCP8.5 – CTRL, shaded, interval 0.1 PSU) during DJF (top
1001 row) and JJA (bottom row) in (a) (d) GFDL-ROMS, (b) (e) IPSL-ROMS, and (c) (f) HadGEM-
1002 ROMS. The 200m isobath is indicated by the black curve.
1003

1004 Fig. 7. Cross section of the annual mean temperature (top) and salinity (bottom) along the
1005 Laurentian Channel in ROMS. Shown are the temperature from CTRL (contour, interval 1.0
1006 °C) and the response (shaded, interval 0.5 °C) and salinity from the CTRL (contour, interval
1007 0.5 PSU) and the response (shaded, interval 0.1 PSU) in (a) (d) GFDL-ROMS, (b) (e) IPSL-
1008 ROMS, and (c) (f) HadGEM -ROMS. Note the section is along the bottom of channel (not a
1009 straight line) and extends from the southeast to northwest, from (A) to (B) in Fig. 1.
1010

1011 Fig. 8. Cross section of the annual mean temperature (top) and salinity (bottom) into the Gulf
1012 of Maine in ROMS. Shown are the temperature from CTRL (contour, interval 1.0 °C) and the
1013 response (shaded, interval 0.5 °C) and salinity from the CTRL (contour, interval 0.25 PSU)
1014 and the response (shaded, interval 0.05 PSU) in (a) (d) GFDL-ROMS, (b) (e) IPSL-ROMS,
1015 and (c) (f) HadGEM-ROMS. Note the section is in the deepest part of the Gulf (not a straight
1016 line) and extends from east to west, from (C) to (D) in Fig. 1.

1017
1018 Fig. 9. Cross section of the annual mean temperature (top) and salinity (bottom) along 28 °N
1019 in the Northern Gulf of Mexico in ROMS. Shown are the temperature from CTRL (contour,
1020 interval 1.0 °C) and the response (shaded, interval 0.5 °C) and salinity from the CTRL (contour,
1021 interval 0.5 PSU) and the response (shaded, interval 0.075 PSU) in (a) (d) GFDL-ROMS, (b)
1022 (e) IPSL-ROMS, and (c) (f) HadGEM-ROMS.

1023
1024 Fig. 10. Static stability, derived from the density difference between 100 m and the surface, in
1025 the CTRL (contours, interval 0.25 kg m⁻³) and the static stability response (RCP8.5-CTRL,
1026 shaded, interval 0.025 kg m⁻³) in ROMS during DJF (top row) and JJA (bottom row) in (a) (d)
1027 GFDL-ROMS, (b) (e) IPSL-ROMS, and (c) (f) HadGEM-ROMS.

1028
1029 Fig. 11. Surface current response (RCP8.5 – CTRL, speed shown by shading, interval 5.0 cm
1030 s⁻¹, vector scale shown in lower right panel) in ROMS during DJF (top row) and JJA (bottom
1031 row) in (a) (d) GFDL-ROMS, (b) (e) IPSL-ROMS, and (c) (f) HadGEM-ROMS.

1032
1033 Fig. 12. Cross section of the annual mean meridional velocity along 30°N in the western North
1034 Atlantic (see Fig. 1) in ROMS. Shown are the velocity from the CTRL (contours, interval 10
1035 cm s⁻¹) and the response (RCP8.5 – CTRL, shading, interval 2.5 cm s⁻¹) in (a) (d) GFDL-
1036 ROMS, (b) (e) IPSL-ROMS, and (c) (f) HadGEM-ROMS.

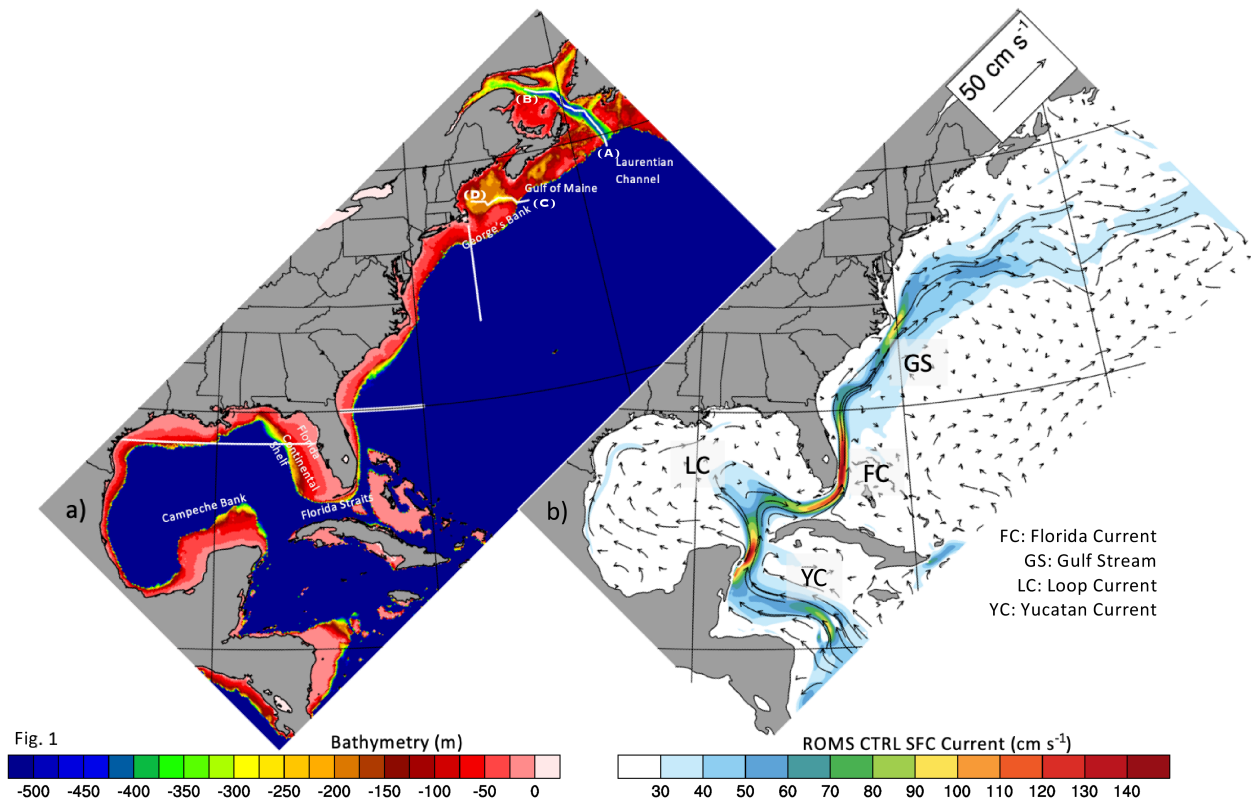
1037
1038 Fig. 13. Annual mean surface current off the northeast US coast in the (a) CTRL (2.5 cm s⁻¹
1039 shading interval), and the current response (RCP8.5 – CTRL, shaded, interval 0.25 cm s⁻¹) in
1040 (b) GFDL-ROMS, (c) IPSL-ROMS and (d) HadGEM-ROMS.

1041
1042 Fig. 14. Cross section of the annual mean meridional velocity along 70°W in the western North
1043 Atlantic (see Fig. 1) in ROMS. Shown are the velocity from the CTRL (contours, interval 5
1044 cm s⁻¹) and the response (RCP8.5 – CTRL, shading, interval 2.5 cm s⁻¹) in (a) GFDL-ROMS,
1045 (b) IPSL-ROMS, and (c) HadGEM-ROMS.

1046
1047 Fig. 15. Surface eddy kinetic energy (EKE) in the CTRL (contours, interval 250 cm² s⁻² starting
1048 at 500) and the EKE response (RCP8.5-CTRL, shaded, interval 25 cm² s⁻²) in ROMS during
1049 DJF (top row) and JJA (bottom row) in (a) (d) GFDL-ROMS, (b) (e) IPSL-ROMS, and (c) (f)
1050 HadGEM-ROMS. The EKE is computed by removing 120-day running mean from the 5-day
1051 average velocity.

1052
1053 Fig. 16. Cross section along 70°W of the response of zonal currents (contours, negative values
1054 are easterly) and salinity (shaded, interval 0.05 PSU) to climate change forcing in the three
1055 ROMS simulations during (a)-(c) DJF and (d)-(f) JJA and for the corresponding GCM

1056 simulations during (g)-(i) DJF and (j-l) JJA. Note the contour interval is 10 cm s^{-1} in ROMS
1057 and 0.5 cm s^{-1} in the GCMS, the top and bottom two rows respectively.
1058



1059
1060
1061
1062
1063
1064
1065
1066
1067

Fig. 1. ROMS domain with (a) bathymetry (shaded, 25 m interval) at 1.85 km resolution. White lines/transects depict the locations of cross-sections shown for the Laurentian Channel (Fig. 7), Gulf of Maine (Fig. 8), 28°N in the Gulf of Mexico (Fig. 9), 30°N east of Florida (Fig. 12), and 70°W south of Cape Cod (Figs. 14 and 16). (b) Annual mean surface currents (shaded, interval 10 cm s^{-1} , vector scale top of right panel) from the ROMS control (CTRL) experiment.

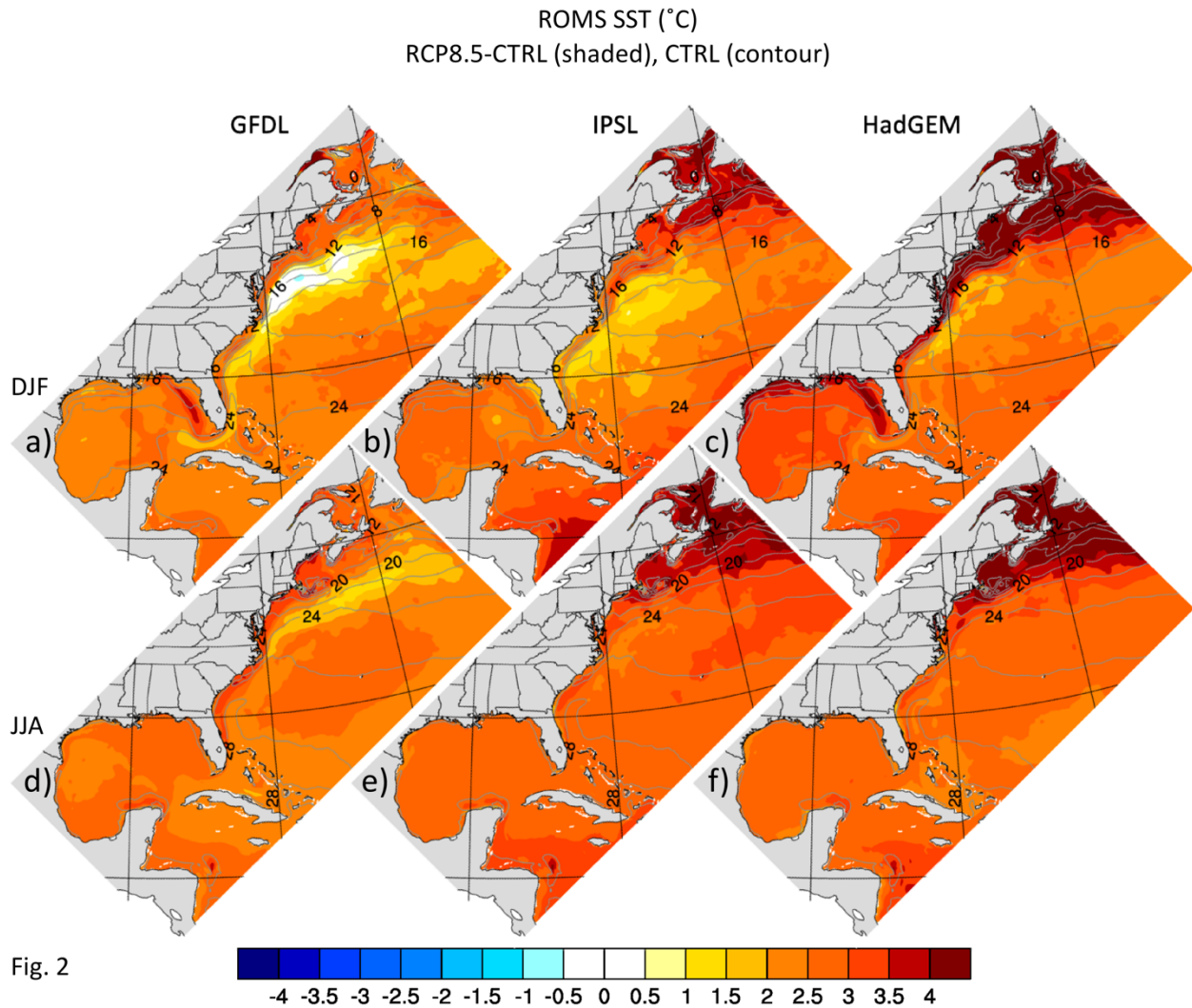
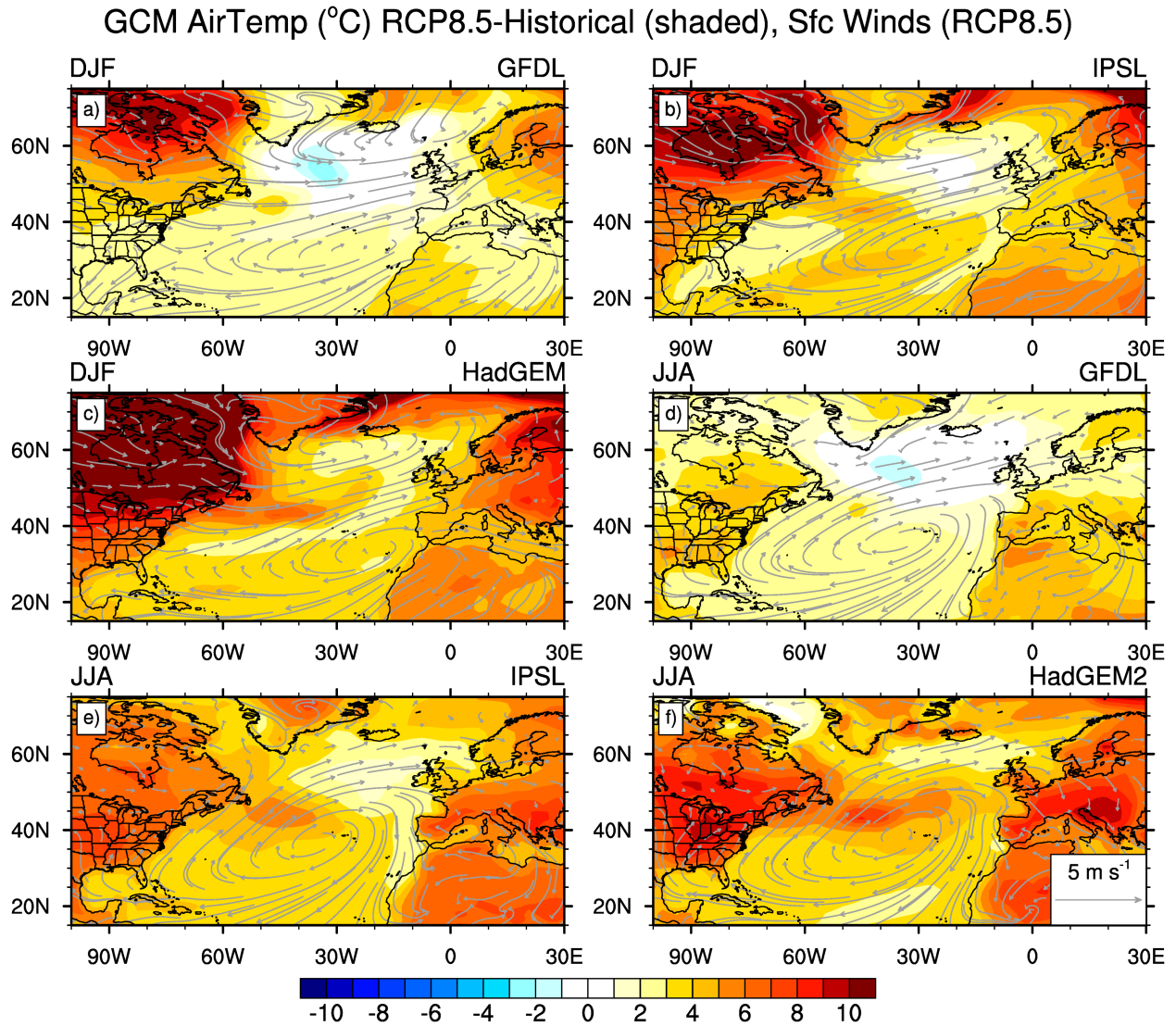


Fig. 2

1068
1069
1070
1071
1072
1073
1074
1075
1076
1077
1078

Fig. 2. SST in the CTRL (contours, interval 2°C) and the SST response to climate change (RCP8.5 – CTRL, shaded, interval 0.5°C) during DJF (top row) and JJA (bottom row) in ROMS driven by three GCMs, i.e. (a) (d) GFDL-ROMS, (b) (e) IPSL-ROMS, and (c) (f) HadGEM-ROMS. The surface and boundary conditions for the CTRL are obtained from reanalysis during 1976-2005 (historical period), with additional forcing added to the CTRL that is derived from the mean difference between 2070-2099 and 1976-2005 in the three RCP8.5 experiments.



1080
 1081
 1082
 1083
 1084
 1085
 1086
 1087
 1088

Fig. 3. Surface air temperature change (RCP8.5 – historical period, shaded 1.0 °C interval) and the surface winds in the RCP8.5 simulations from 2070-2099 (vectors, scale bottom right) during DJF (top) and JJA (bottom) in the (a) (d) GFDL, (b) (e) IPSL, and (c) (f) HadGEM GCMs. This figure highlights how enhanced warming over North America, especially over Canada in winter, could be advected by the winds warming the coastal ocean in the future.

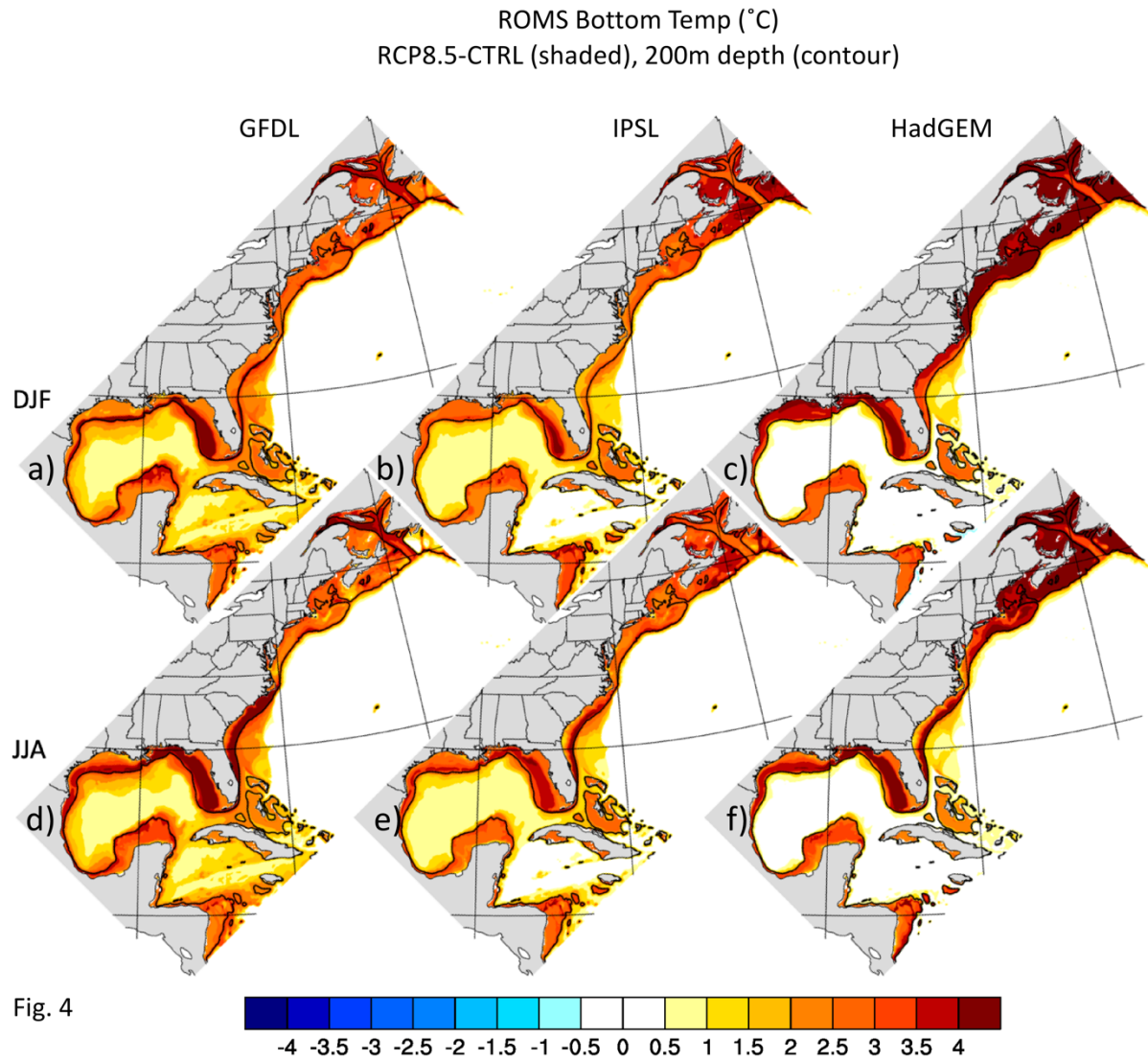


Fig. 4

1089
1090
1091
1092
1093
1094
1095
1096

Fig. 4. Bottom temperature response (RCP8.5 – CTRL, shaded, interval 0.5 °C) during DJF (top row) and JJA (bottom row) in (a) (d) GFDL-ROMS, (b) (e) IPSL-ROMS, and (c) (f) HadGEM-ROMS. The 200m isobath, representing the shelf break, is indicated by the black curve.

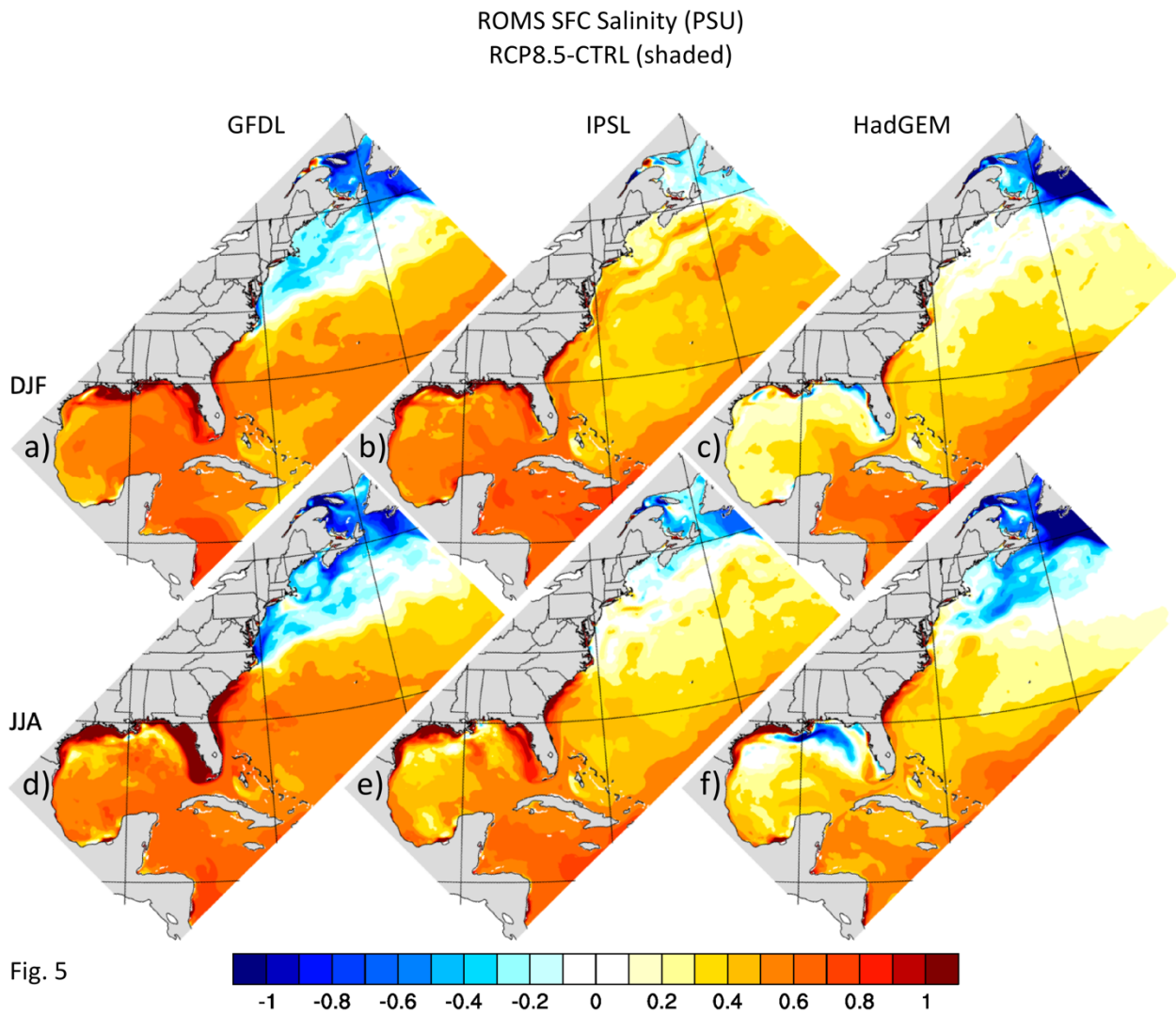


Fig. 5

1097
1098
1099
1100
1101
1102
1103
1104
1105

Fig. 5. Sea surface salinity (SSS) response (RCP8.5 – CTRL, shaded, interval 0.1 PSU) during DJF (top row) and JJA (bottom row) in (a) (d) GFDL-ROMS, (b) (e) IPSL-ROMS, and (c) (f) HadGEM -ROMS.

ROMS Bottom Salinity (PSU)
RCP8.5-CTRL (shaded), 200m depth (contour)

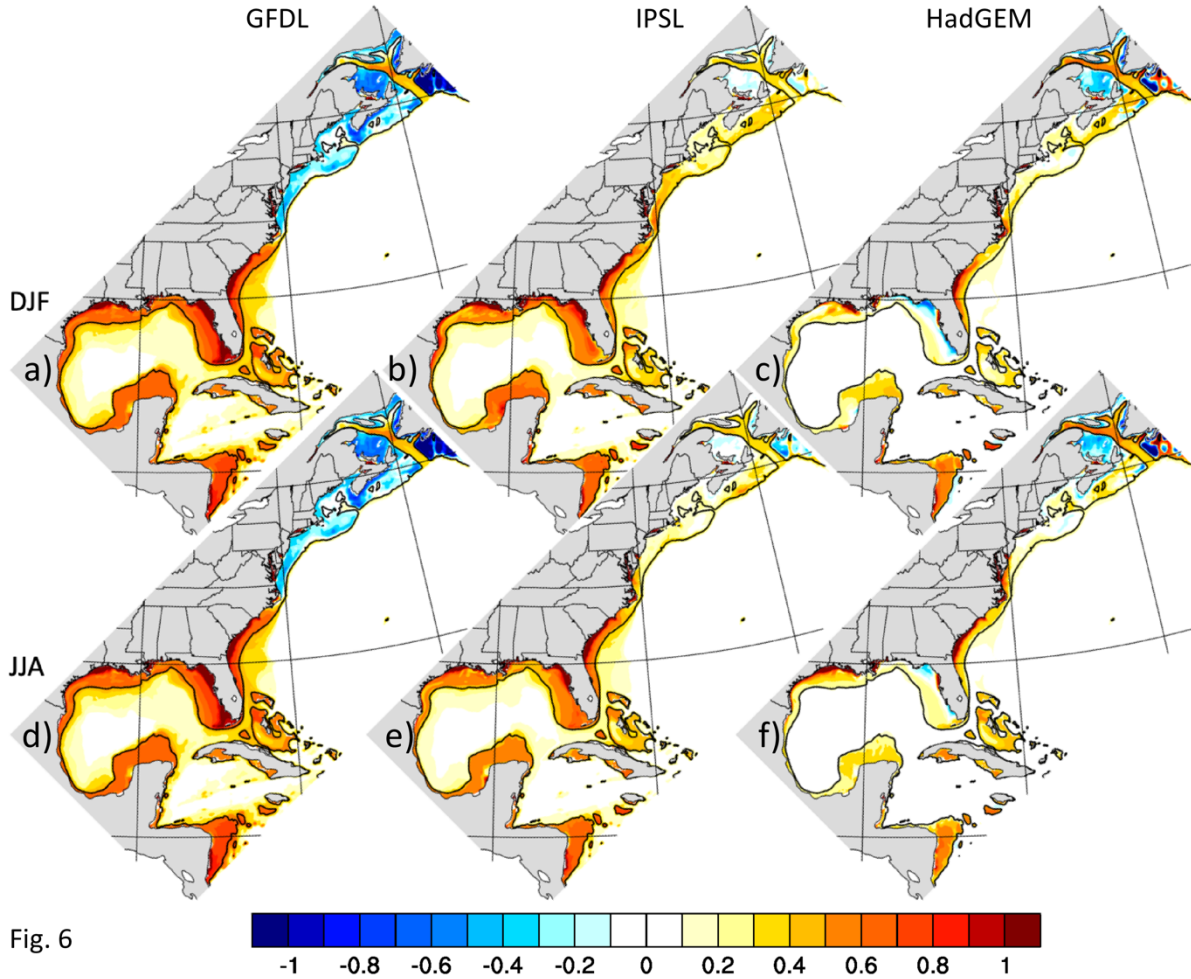


Fig. 6

1106
1107
1108
1109
1110
1111
1112
1113
1114

Fig. 6. Bottom salinity response (RCP8.5 – CTRL, shaded, interval 0.1 PSU) during DJF (top row) and JJA (bottom row) in (a) (d) GFDL-ROMS, (b) (e) IPSL-ROMS, and (c) (f) HadGEM-ROMS. The 200m isobath is indicated by the black curve.

ROMS Laurentian Channel X-section Annual Mean
RCP8.5-CTRL (shaded), CTRL (contour)
TEMP (°C)

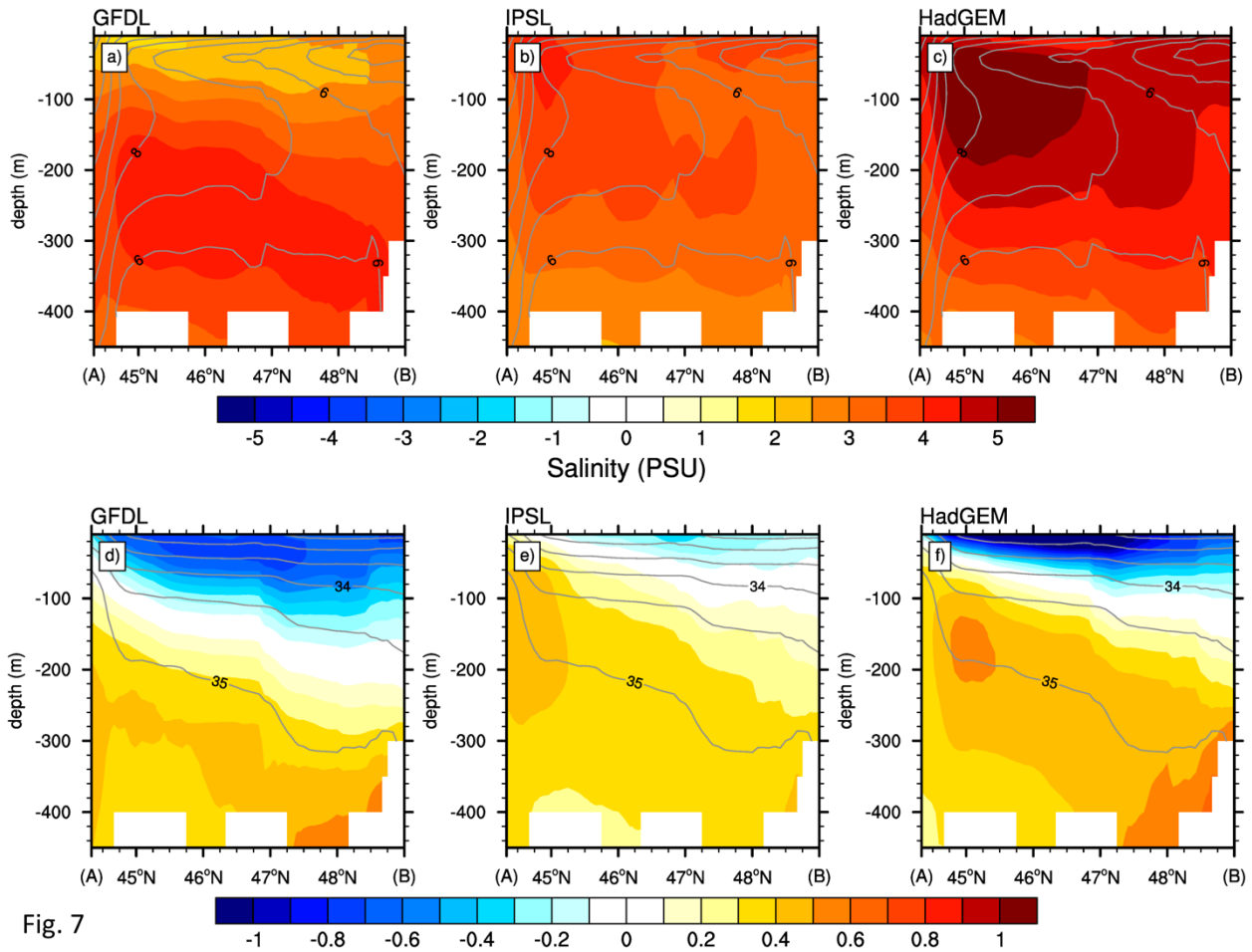


Fig. 7

1115
1116
1117
1118
1119
1120
1121
1122
1123
1124
1125
1126

Fig. 7. Cross section of the annual mean temperature (top) and salinity (bottom) along the Laurentian Channel in ROMS. Shown are the temperature from CTRL (contour, interval 1.0 °C) and the response (shaded, interval 0.5 °C) and salinity from the CTRL (contour, interval 0.5 PSU) and the response (shaded, interval 0.1 PSU) in (a) (d) GFDL-ROMS, (b) (e) IPSL-ROMS, and (c) (f) HadGEM -ROMS. Note the section is along the bottom of channel (not a straight line) and extends from the southeast to northwest, from (A) to (B) in Fig. 1.

ROMS Gulf of Maine X-section Annual Mean
RCP8.5-CTRL (shaded), CTRL (contour)
TEMP (°C)

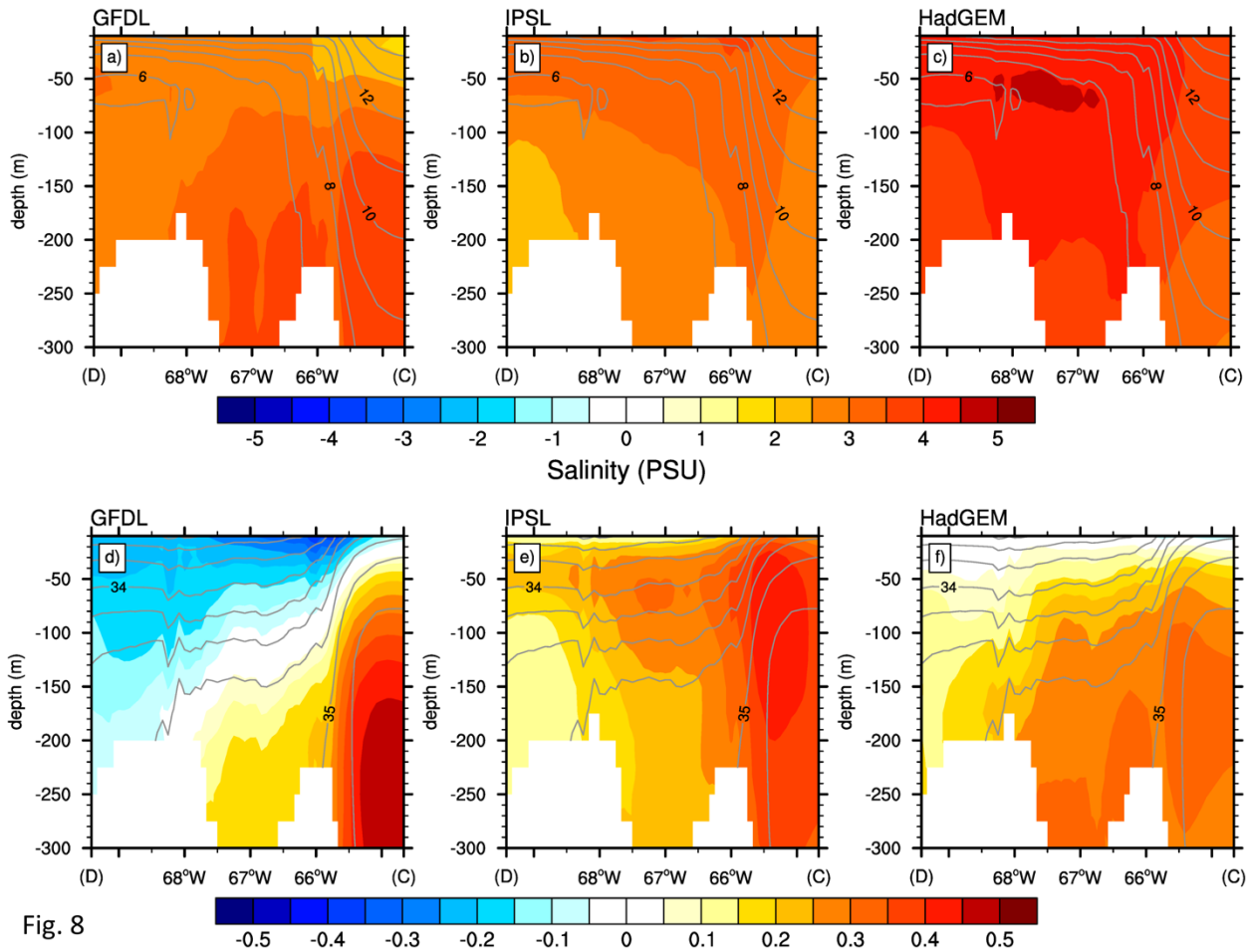


Fig. 8

1127
1128
1129
1130
1131
1132
1133
1134
1135
1136
1137
1138

Fig. 8. Cross section of the annual mean temperature (top) and salinity (bottom) into the Gulf of Maine in ROMS. Shown are the temperature from CTRL (contour, interval 1.0 °C) and the response (shaded, interval 0.5 °C) and salinity from the CTRL (contour, interval 0.25 PSU) and the response (shaded, interval 0.05 PSU) in (a) (d) GFDL-ROMS, (b) (e) IPSL-ROMS, and (c) (f) HadGEM-ROMS. Note the section is in the deepest part of the Gulf (not a straight line) and extends from east to west, from (C) to (D) in Fig. 1.

ROMS Gulf of Mexico (28°N) X-section Annual Mean
RCP8.5-CTRL (shaded), CTRL (contour)
TEMP (°C)

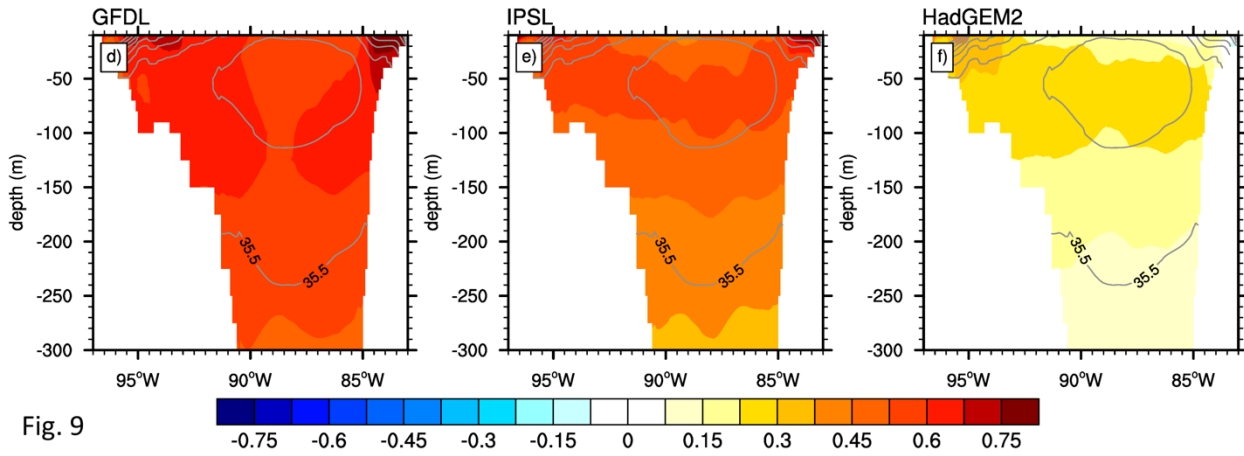
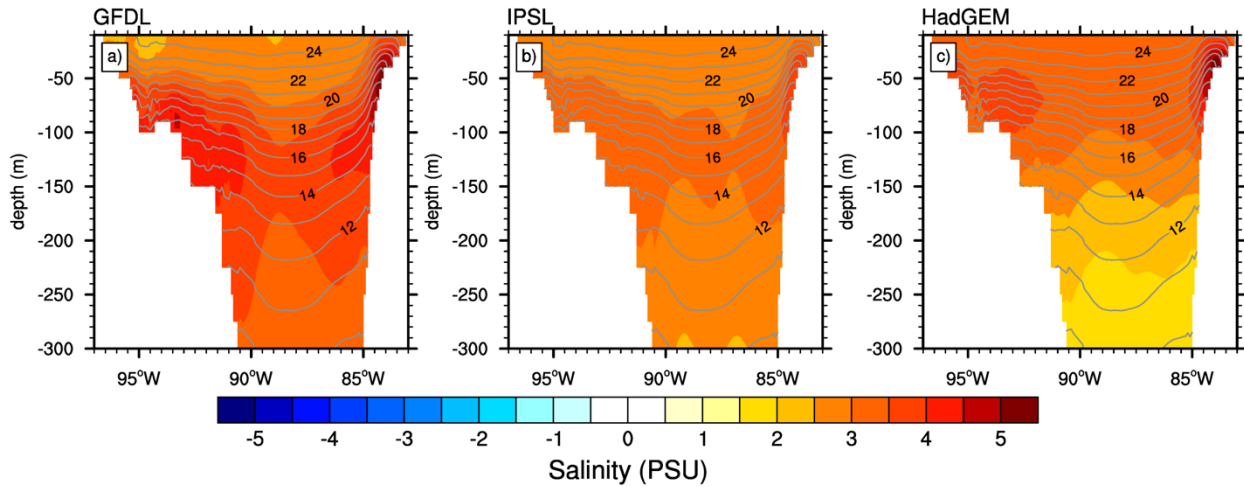


Fig. 9

1139
1140
1141
1142
1143
1144
1145
1146
1147
1148

Fig. 9. Cross section of the annual mean temperature (top) and salinity (bottom) along 28°N in the Northern Gulf of Mexico in ROMS. Shown are the temperature from CTRL (contour, interval 1.0 °C) and the response (shaded, interval 0.5 °C) and salinity from the CTRL (contour, interval 0.5 PSU) and the response (shaded, interval 0.075 PSU) in (a) (d) GFDL-ROMS, (b) (e) IPSL-ROMS, and (c) (f) HadGEM-ROMS.

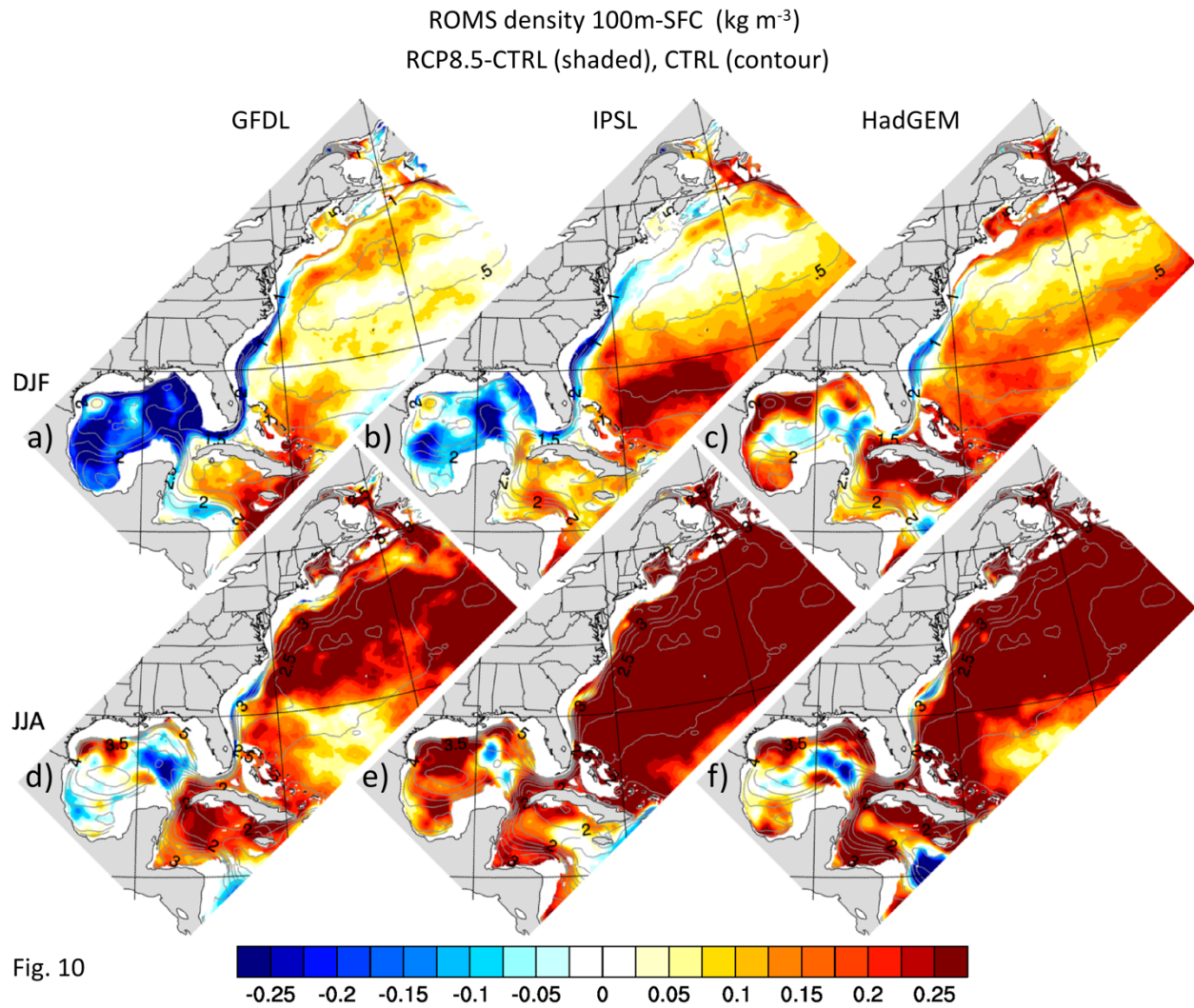
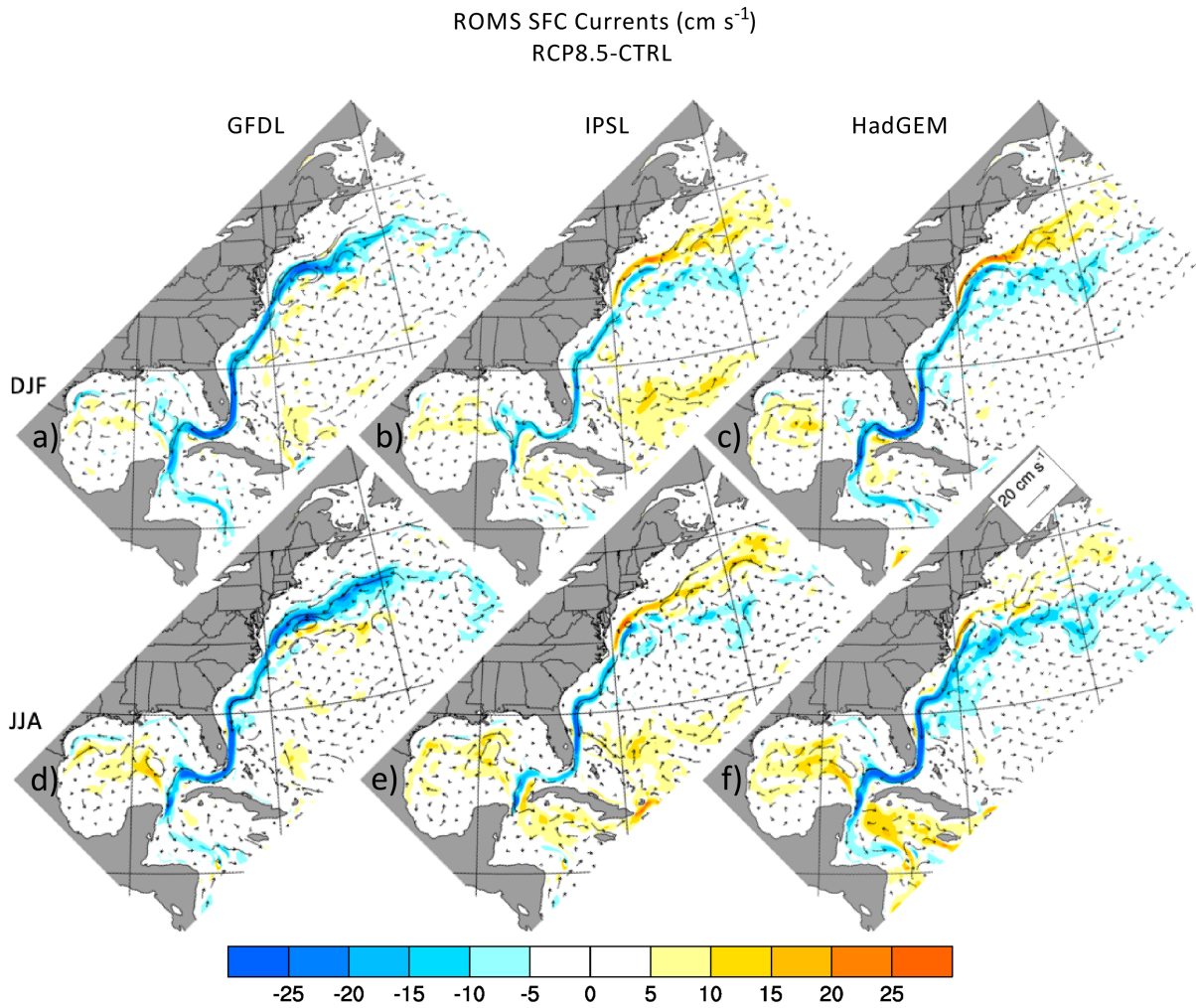


Fig. 10

1149
1150
1151
1152
1153
1154
1155
1156
1157
1158

Fig. 10. Static stability, derived from the density difference between 100 m and the surface, in the CTRL (contours, interval 0.25 kg m^{-3}) and the static stability response (RCP8.5-CTRL, shaded, interval 0.025 kg m^{-3}) in ROMS during DJF (top row) and JJA (bottom row) in (a) (d) GFDL-ROMS, (b) (e) IPSL-ROMS, and (c) (f) HadGEM-ROMS.



1160
1161
1162
1163
1164
1165
1166
1167

Fig.11. Surface current response (RCP8.5 – CTRL, speed shown by shading, interval 5.0 cm s^{-1} , vector scale shown in lower right panel) in ROMS during DJF (top row) and JJA (bottom row) in (a) (d) GFDL-ROMS, (b) (e) IPSL-ROMS, and (c) (f) HadGEM-ROMs.

ROMS (30°N) X-section Annual Mean
RCP8.5-CTRL (shaded), CTRL (contour)
Ocean Meridional Velocity (cm s^{-1})

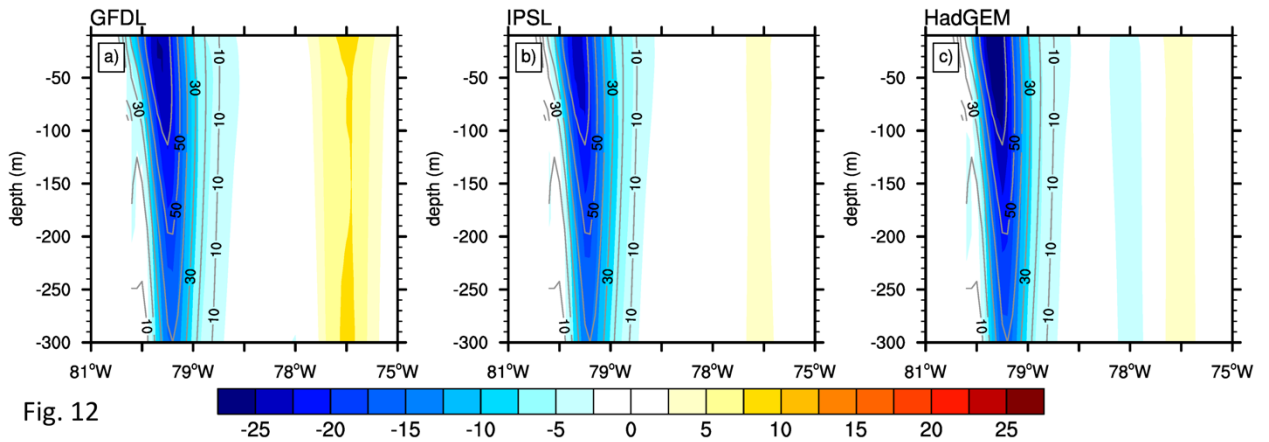
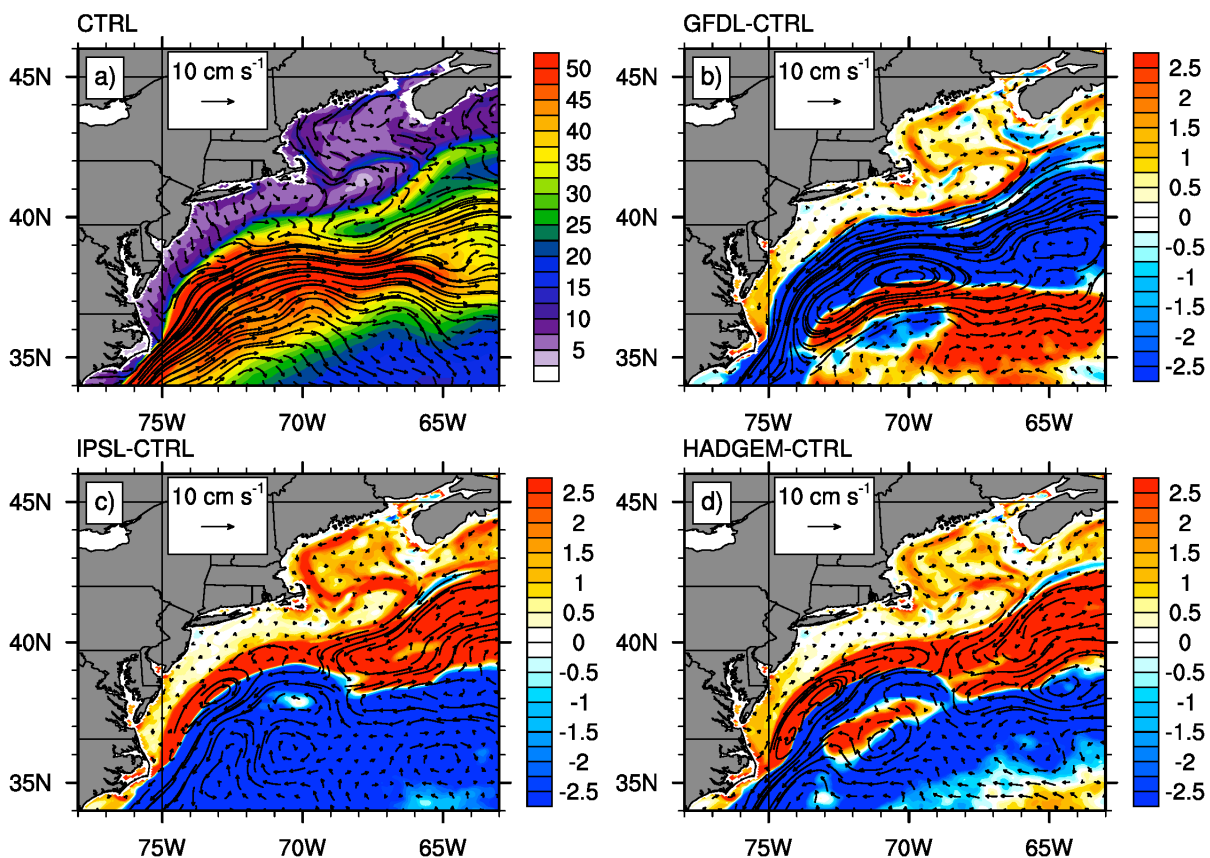


Fig. 12

1168
1169
1170
1171
1172
1173
1174
1175
1176
1177

Fig. 12. Cross section of the annual mean meridional velocity along 30°N in the western North Atlantic (see Fig. 1) in ROMS. Shown are the velocity from the CTRL (contours, interval 10 cm s^{-1}) and the response (RCP8.5 – CTRL, shading, interval 2.5 cm s^{-1}) in (a) (d) GFDL-ROMS, (b) (e) IPSL-ROMS, and (c) (f) HadGEM-ROMS.

ROMS Sfc Current Annual Mean (cm s^{-1})



1178
 1179
 1180
 1181
 1182
 1183
 1184
 1185
 1186

Fig. 13. Annual mean surface current off the northeast US coast in the (a) CTRL (2.5 cm s^{-1} shading interval), and the current response (RCP8.5 - CTRL, shaded, interval 0.25 cm s^{-1}) in (b) GFDL-ROMS, (c) IPSL-ROMS and (d) HadGEM-ROMS.

ROMS (70°W) X-section Annual Mean
RCP8.5-CTRL (shaded), CTRL (contour)
ROMS Ocean Zonal Velocity (cm s^{-1})

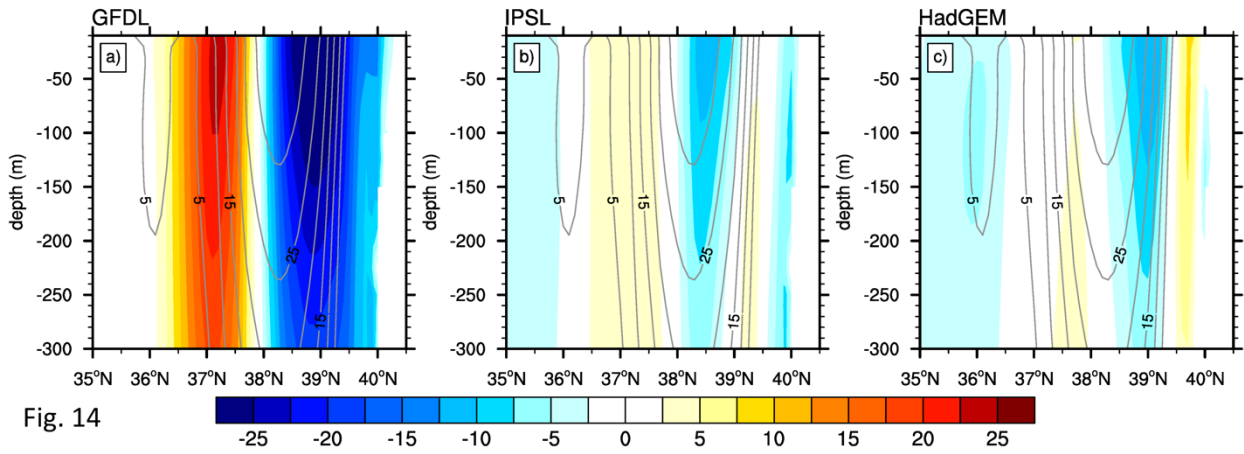
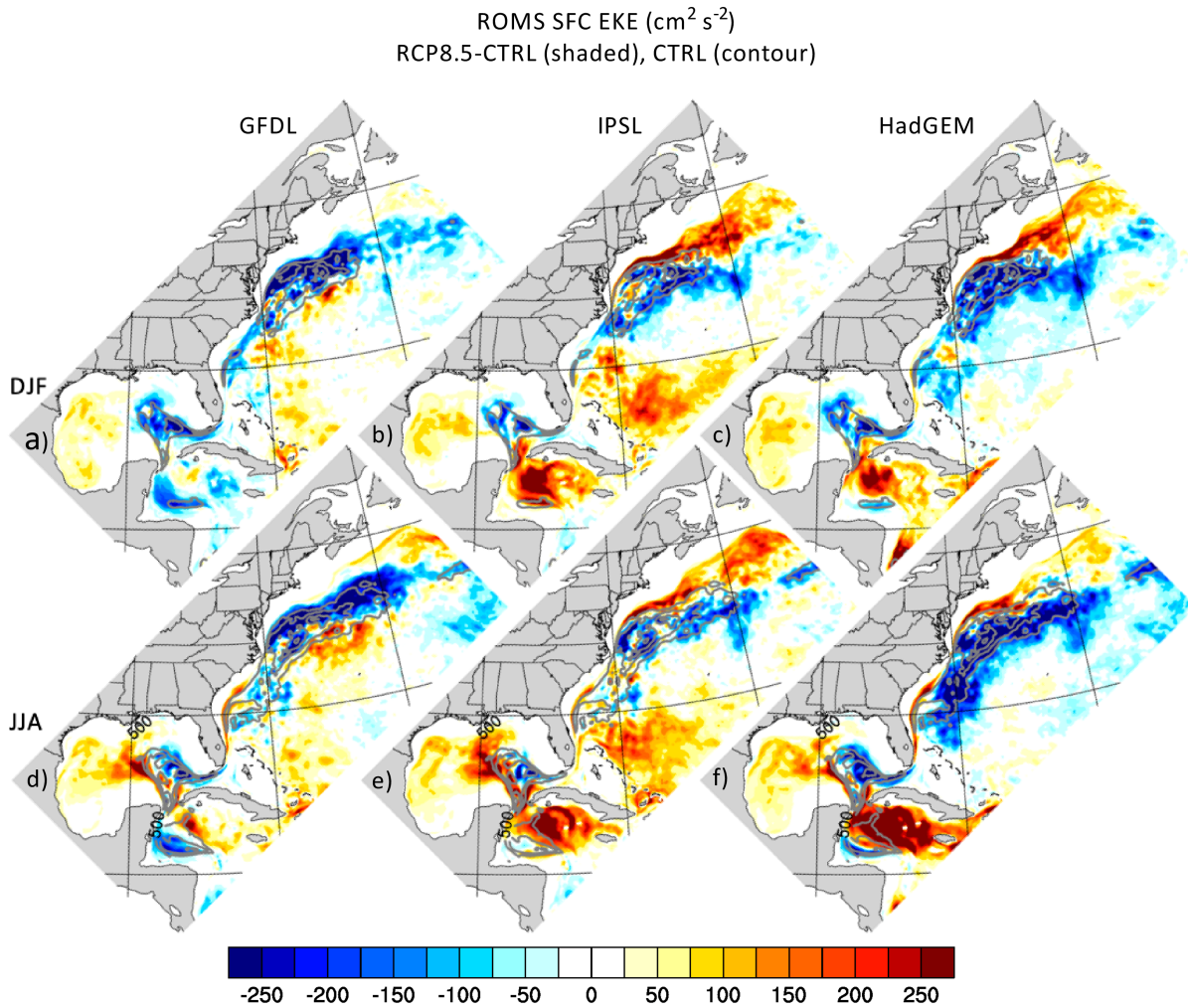


Fig. 14

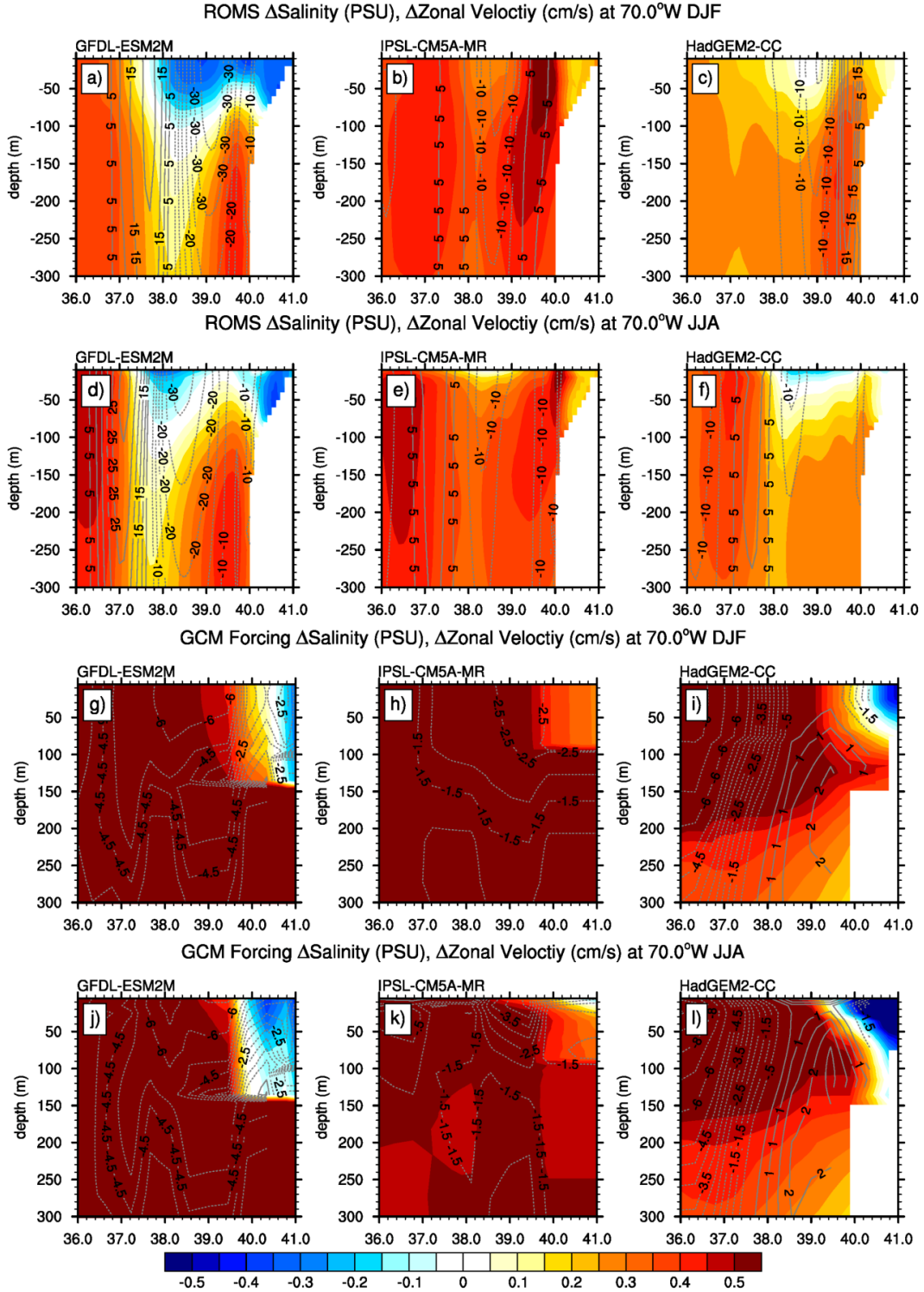
1187
1188
1189
1190
1191
1192
1193
1194
1195
1196

Fig. 14. Cross section of the annual mean meridional velocity along 70°W in the western North Atlantic (see Fig. 1) in ROMS. Shown are the velocity from the CTRL (contours, interval 5 cm s^{-1}) and the response (RCP8.5 - CTRL, shading, interval 2.5 cm s^{-1}) in (a) GFDL-ROMS, (b) IPSL-ROMS, and (c) HadGEM-ROMS.



1197
1198
1199
1200
1201
1202
1203
1204
1205
1206
1207

Fig. 15. Surface eddy kinetic energy (EKE) in the CTRL (contours, interval $250 \text{ cm}^2 \text{ s}^{-2}$ starting at 500) and the EKE response (RCP8.5-CTRL, shaded, interval $25 \text{ cm}^2 \text{ s}^{-2}$) in ROMS during DJF (top row) and JJA (bottom row) in (a) (d) GFDL-ROMS, (b) (e) IPSL-ROMS, and (c) (f) HadGEM-ROMS. The EKE is computed by removing 120-day running mean from the 5-day average velocity.



1208
 1209
 1210
 1211
 1212
 1213
 1214

Fig. 16. Cross section along 70°W of the response of zonal currents (contours, negative values are easterly) and salinity (shaded, interval 0.05 PSU) to climate change forcing in the three ROMS simulations during (a)-(c) DJF and (d)-(f) JJA and for the corresponding GCM simulations during (g)-(i) DJF and (j-l) JJA. Note the contour interval is 10 cm s⁻¹ in ROMS and 0.5 cm s⁻¹ in the GCMS, the top and bottom two rows, respectively.